Is *nothing* a sphere?
Investigating the assumptions of the
Alcock-Paczyński test for voids

Author:
Błażej ROZMARYNOWICZ
(s4863852)

Supervisor:
prof. Rien VAN DE WEYGAERT
Second examiner :
prof. Eric BERGSHOEFF

Bachelor's Thesis
To fulfill the requirements for the degree of
Bachelor of Science in Physics
at the University of Groningen

July 10, 2024

Contents

Abstract

In recent years, parts of the cosmological community have decided to approach the Hubble tension debate from a new angle, one focused on the study of cosmic voids. These large, underdense regions provide a perfect 'laboratory', in which research of dark energy, dark matter and neutrinos can flourish. Due to their relative emptiness, the dynamics of these voids are largely defined by their interactions with their external environments, be it through tidal fields or void-to-void interactions, which can lead to their preferred shapes and orientations. Amongst others, Ryden and Lavaux argue cosmic voids can be stacked on top of each other to artificially build a perfect sphere given local isotropy and large void quantities [1][2]. This would allow voids to be applied to the Alcock-Paczyński test, significantly constraining the Hubble tension. In this thesis, we investigate the shape of voids on a local scale, focusing on a $L = 106.5 \text{Mpc} h^{-1}$ box of dark-matter particles from the Illustris-3-Dark simulation. The particle distribution is analysed in both physical and redshift space across 10 timesteps. We use DTFE and WVF density field tessellation and void identification methods to mark the voids, subsequently parametrizing them as ellipsoids with a characteristic ellipticity (ε), prolateness (α) and volume (V).

In our investigation, we find that the average stacked void is not perfectly spherical for a small range of redshifts, when binned by volume and depth. We also find that the application of these voids in the Alcock-Paczyński test results in nonsensical values of $e_v(z)$, however these results are not statistically significant due to multiple biases inherent in the chosen methods, as well as a general lack of data. Finally, we find that the chosen parametrization of voids results in volume fraction significantly larger than those present in the literature. We suggest further study into the fundamental assumptions of void use in the Alcock-Paczyński test, pushing the field forwards with confidence, rather than uncertainty.

Acknowledgments

1   INTRODUCTION

The study of cosmology is fraught with uncertainty. While this is largely the case in any scientific field, only a some of them have gone through as many paradigm shifts over the last century as cosmology. It is truly astounding that although the fundamentals of investigating the cosmos have stayed mostly the same for a long time - at the end of the day, most studies are based on simple observation, we still find new, exciting phenomena in our cosmic backyard. From super-massive black holes to dark energy and matter, it seems that no matter where we look, we manage to find *something* that questions our theories and assumptions. A more recent development - researchers have found that **about** 5% of what we can see in the sky is ordinary matter [3]. The seemingly infinite number of stars, planets and galaxies, illuminating the night sky constitute only a small fraction of what is truly out there. What about the other 95%?

It is a combination dark energy, exerting a kind of negative pressure on the fabric of space-time, and dark matter, which behaves in all the ways ordinary matter does, except, it is seemingly *invisible*. This, intuitively, sounds ridiculous. The mere existence of both of these phenomena throws a super-sized wrench into the delicate machinery of our cosmological theories. However, aside from abandoning General Relativity for a version of modified gravity [5], the only explanation that accurately accounts for the strange findings of cosmological observations are these elusive concepts. Adding onto the pile, the cosmological community has been in disagreement about a number of fundamental properties of the universe, like its rate of expansion [6], making for a truly hectic research environment. How do we 'find' matter that is invisible, the energy, whose sole purpose is furthering the separa-

Figure 1: 3D visualization of the Local Void. From Hidding *et al.*[4].

tion between us and the celestial bodies we observe? How can we identify the parameters, which help accurately describe at what rate that separation increases? In the midst of this chaos, some researchers turned away from looking at regions of overflowing visible density, and turned to the study of vast regions of *nothing* - cosmic voids.

1.1   Making something out of nothing

While voids, defined as large regions of underdensity [7], have been known to exist for almost half a century [8], it is only recently that they attracted the attention of the cosmological community at large. Before we get ahead of ourselves however, we first need to address why studying regions of relative emptiness would be useful at all. In philosophy, it is incredibly useful to consider hypothetical scenarios that can serve as tests of our beliefs. More often than not, these 'hypotheticals' are deliberately extreme, to the point of being unrealistic. However, this extremity is exactly the point - hypotheticals allow us to isolate certain variables, focusing us on the study of what is at the heart of any philosoph-

ical question. Voids serve a similar purpose, with the huge benefit of, contrary to hypotheticals, not being made-up. Observing regions of vast empty space isolates both the influence of dark energy *and* dark matter, which can now exist in an environment bereft of ordinary matter [9]! Looking at the distribution of matter in the universe, we can liken it to a cosmic 'web' - filled with visible filaments, clusters and walls, punctured with 'holes' denoting cosmic voids. Like a fishnet-covered balloon, we can imagine the voids rapidly expanding seemingly on their own as a sheer byproduct of the expansion of space in which they are nested! Another benefit of voids is their sheer volume, quite literally in fact, as voids have been found to constitute up to 77% of cosmic web environments [10][7], hence they are very easy to find and identify by eye.
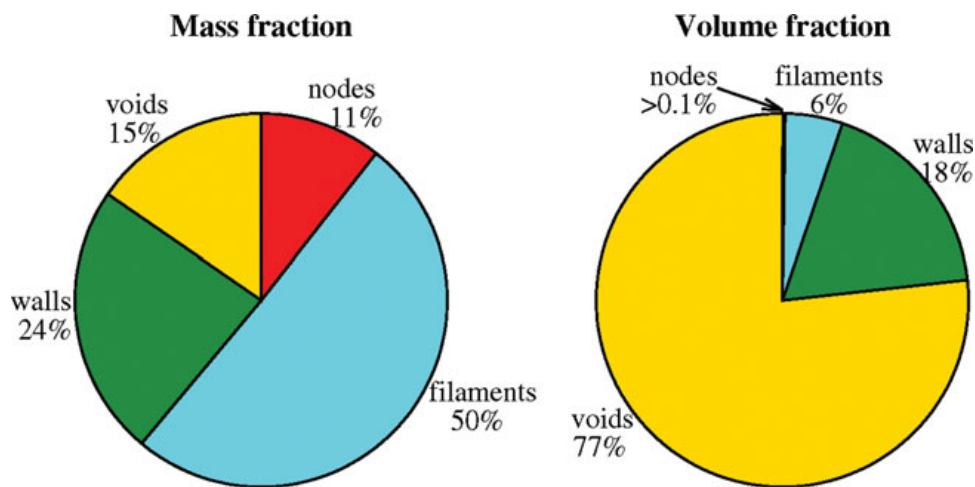

Figure 2: Mass and volume fractions of cosmic web constituents found with the NEXUS+ method. From Cautun *et al.* [10].

1.2   The perfect cosmological probe?

As we insinuated beforehand, voids may also hold the key to answering the question of the rate at which the universe expands [1]. This is no simple matter, as we later explain in 2, the Hubble parameter responsible for describing this rate *changes* with time. Add onto that the fact that all observational data we can gather is distorted, as the light from celestial bodies travels as a finite speed and hence is subject to stretching due to the expansion, and we see that any simple consideration of the change in velocity of observed bodies is not sufficient in determining the Hubble parameter. Voids however, may prove to be incredibly useful thanks to their vastness and lack of contents. Because the universe seems to be largely homogeneous and isotropic, as supported by, e.g. CMB data, we can expect the average void to be purely spherical. Coincidentally, one of the most accurate test that can be used to determine the current Hubble constant, the Alcock-Paczyński test [11], relies on observing the distortion of a body that is known to be spherical in physical space.

However, it is difficult to simply 'take all the voids' in the universe and stack them together - cosmological observations are often limited in scope and time, hence constructing this perfect probe proves no easy task. Nonetheless, some researchers already grasped the promise held by voids and seemingly rushed into the fray of the Hubble tension assuming that stacking enough voids on smaller scales will similarly result in a perfect sphere. While we certainly hope this is the case, assumptions like these should *always* be double-checked, lest we disappoint ourselves by finding out our solutions to the mysteries of the cosmos were built on shaky foundations.
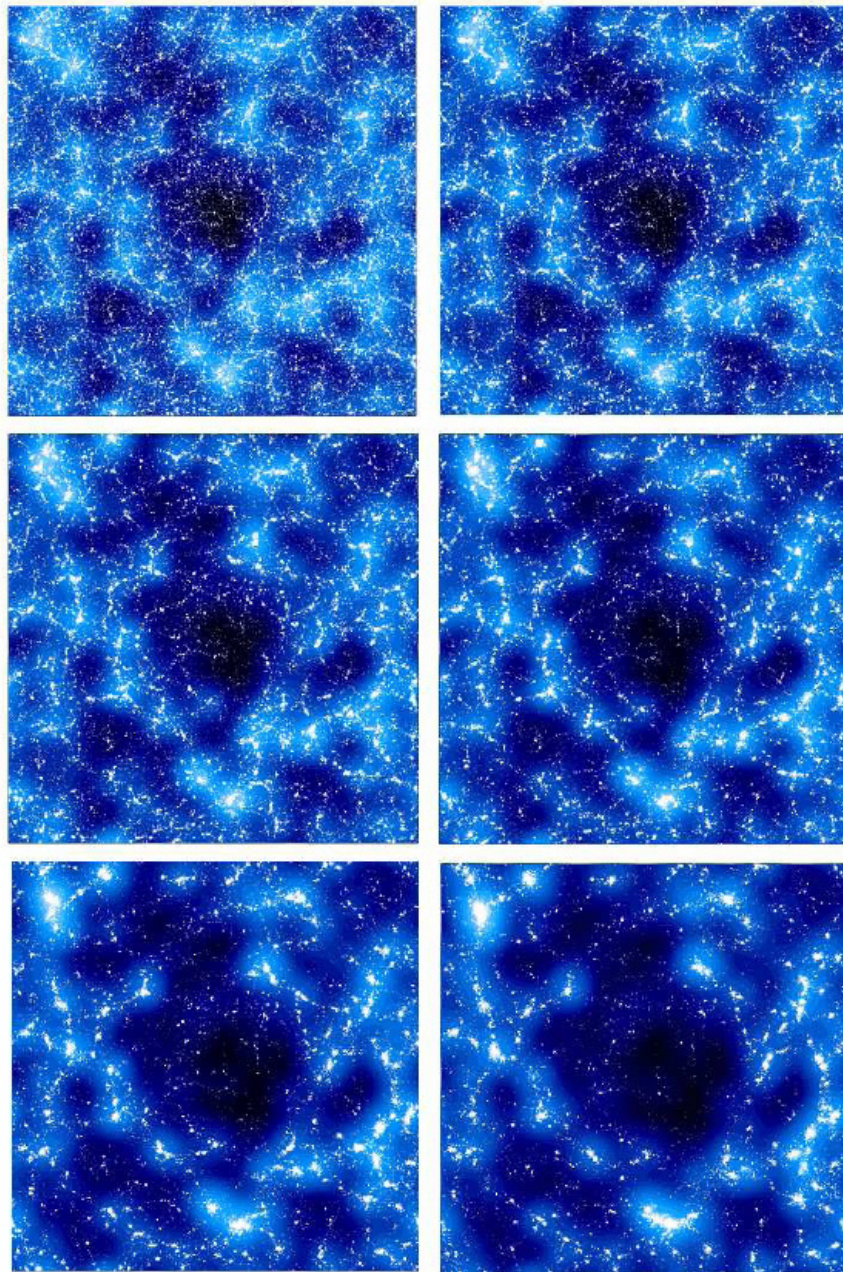
Figure 3: Evolution of a ΛCDM void. Slices correspond to a width of 50Mpch^{-1} and thickness of 10Mpch^{-1}, across six timesteps $a = \{0.05, 0.15, 0.35, 0.55, 0.75, 1.0\}$. From van de Weygaert [7].

1.3   Research Questions

In this thesis, we investigate the shape of voids using a Illustris simulation data, and apply our results to the Alcock-Paczyński test. We aim to answer the following questions:

1. Is the average (stacked) void spherical?

2. Can slightly aspherical voids be applied in the Alcock-Paczyński test?

3. Does the ellispoidal parametrization of voids accurately reflect their true volumes?

2   FRWL cosmology

Before delving deeper into the world of voids, we first introduce a couple key concepts necessary for a comprehensive understanding of the context, in which all later analysis is rooted.

2.0.1   The Cosmological Principle

The universe is homogeneous and isotropic on large enough scales - for year now this notion has been the defining 'principle' behind the impetus of modern cosmology. While this assumption is patently untrue for local regions, the principle almost holds for scales comparable to the Hubble length, $L_H \approx 4000 \text{Mpc}$, [12] and hence works as a very useful heuristic for constraining degrees of freedom in cosmological research. Indeed, the principle allows for an exact solution to the famous Einstein Field Equations

$$R_{\mu\nu} - \frac{1}{2}g_{\mu\nu}R + g_{\mu\nu}\Lambda = \frac{8\pi G}{c^4}T_{\mu\nu}, \tag{1}$$

which are key to describing the relationship between space-time curvature and local matter and radiation energy densities [13]. The solution, known as the Friedmann-Lemaitre-Robertson-Walker (FRWL) metric, allows us to find the distance between any two points in curved space-time, following

$$ds^2 = -c^2 dt^2 + a(t)^2[dr^2 + S_\kappa(r)^2 d\Omega^2], \tag{2}$$

with

$$S_k = \begin{cases} R_0 \sin(\frac{r}{R_0}) & (\kappa = 1) \\ r & (\kappa = 0) \\ R_0 \sinh\frac{r}{R_0} & (\kappa = -1), \end{cases} \tag{3}$$

Where κ indicates three distinct space-time geometries: positively-curved, flat, and negatively-curved, respectively. We note the casual use of spherical coordinates (which will surely come up later in the discussion), and define

$$d\Omega^2 \equiv d\theta^2 + \sin^2\theta d\phi^2.$$

While a truly impressive result, we shift our focus to the factor $a(t)$ - the scale factor, which can be fairly said to define this entire investigation.

2.1   Scale factor and Hubble constant

When looking at a distant object in space along a geodesic (shortest path in curved space), using the FRWL metric at a given time, t, we find

$$ds = a(t)dr, \tag{4}$$

and hence the proper distance,

$$d_p(t) = a(t)r, \tag{5}$$

subsequently denoting r as the 'comoving distance', which stays invariant under Hubble expansion. This is because, while homogeneous and isotropic, the universe expands differently throughout time.

The best known quantitative description is ascribed to Edwin Hubble [REF], who, observing the motion of galaxies, found that

$$\mathbf{v} = H(t)\mathbf{r}.^1 \tag{6}$$

We hence have two major factors: the universe is expanding and hence so are distances between points in space, which we can describe with the scale factor $a(t)$; and that galaxies, with the exceptions proving the rule being part of the Local Group, are receding from us with a time-dependent parameter $H(t)$. Connecting the two, we find

$$H(t) \equiv \frac{\dot{a}(t)}{a(t)}. \tag{7}$$

While commonly known as the 'Hubble constant', it is clear that the parameter is not a constant in the slightest. Adding to the confusion, the cosmological community decided on 'little h', as the wiggle-factor in the value of $H(t = 0)$. We will hence denote $H(t = 0) = H_0$ as the Hubble *constant*, taking the convention $H_0 = 100h\,\mathrm{kms}^{-1}\mathrm{Mpc}^{-1}$, and call $H(t \neq 0)$ the Hubble parameter. We may additionally define the acceleration (or deceleration) parameter, q_0, which describes the rate at which the expansion of the universe accelerates

$$q \equiv -\frac{\ddot{a}a}{\dot{a}^2}. \tag{8}$$

Coming back to the FRWL metric, we introduce the Friedmann equations

$$\left(\frac{\dot{a}}{a}\right)^2 = \frac{8\pi G}{3c^2}\varepsilon - \frac{\kappa c^2}{R_0^2 a^2} + \frac{\Lambda}{3},$$
$$\left(\frac{\ddot{a}}{a}\right) = \frac{4\pi G}{3c^2}(\varepsilon + 3P) + \frac{\Lambda}{3},$$

where we denote ε as the energy density, P as pressure, and R_0 as the radius of curvature. Dark energy, described by the cosmological constant, Λ, complicates these equations by the equivalent of adding a component of energy density

$$\varepsilon_\Lambda \equiv \frac{c^2}{8\pi G}\Lambda,$$

which we will expand on shortly. First, we focus on the implications of equation ([EQ REF]). As previous defined, $H(t) = \frac{\dot{a}(t)}{a(t)}$, hence the first equation can be rewritten as

$$H(t)^2 = \frac{8\pi G}{3c^2}\varepsilon - \frac{\kappa c^2}{R_0^2 a^2} + \frac{\Lambda}{3}. \tag{9}$$

Furthermore, we may define the critical density

$$\varepsilon_c \equiv \frac{3c^2}{8\pi G}H(t)^2, \tag{10}$$

which can inform us about the curvature, κ [13]. Finally, we reach the density parameter, defined as

$$\Omega \equiv \frac{\varepsilon}{\varepsilon_c}, \tag{11}$$

---

[1]From now on, we denote vectors, such as $\vec{v}$, in bold-text $\mathbf{v}$.

Where $\Omega_0 = 1$. With this, we may derive a useful equation relating $E(z) = \frac{H(z)}{H_0}$ to the various density parameters as follows

$$E(z) = \sqrt{\frac{\Omega_{m,0}}{a^3} + \frac{1 - \Omega_{m,0} - \Omega_{\Lambda,0}}{a^2} + \Omega_{\Lambda,0}}. \tag{12}$$

2.2   Redshift and measurements

While these theoretical deliberations are all fascinating, we cannot ignore the fundamental question at the heart of cosmology - how do we measure distances to celestial bodies? The question may seem trivial at first, but we remind ourselves that, unfortunately, humanity lacks the ability to measure distance by eye alone, and has not yet build a yardstick long enough to reach distant stars and planets. Furthermore, we note how the definitions presented in (4) and (5) both relate to distance as a fundamental measure. We hence introduce the concept of redshift, z.

2.2.1   Different distortions

We should first begin by asking the question - how do we measure anything in the first place? Generally, the answer is related to light. As the light bounces off a distant object, it reaches Earth after some time, entering the eyes of some poor astronomer, whose brain translates the photons into information. However, as noted before the the universe, and hence the space in which light travels, expands, and hence, so does the wavelength. We hence define the redshift of an object as

$$z \equiv \frac{\lambda_{\text{obs}} - \lambda_{\text{em}}}{\lambda_{\text{em}}} = \frac{\lambda_{\text{obs}}}{\lambda_{\text{em}}} - 1, \tag{13}$$

where λ_{obs}, λ_{em} denote the observed and emitted wavelength, respectively. We can then relate the scale factor 'responsible' for the expansion to the redshift as

$$a(t) = \frac{1}{1 + z}. \tag{14}$$

This brings us one step closer to proper distance measurements! Except, redshift due to the expansion of space-time is not the only type of redshift there is. In general, we categorize redshift as cosmological, Doppler, and gravitational, the last of which we will skip as it is marginal for the purposes of this investigation. The famous Doppler effect relates to the wave distortion cause by the relative movement of the 'emitting' body. While in day-to-day life this is reflected in loud cars passing by pedestrians, the distortion is a particularly insidious factor in the life of a cosmologist. As should be immediately clear, the different types of redshift are essentially indistinguishable by eye, hence decoupling and isolating them is paramount to proper cosmological measurements. To do so, we exploit the definition presented in (14), transforming it slightly, such that

$$z + 1 = \frac{\lambda_{\text{obs}}}{\lambda_{\text{em}}}.$$

Then, we can see that

$$z + 1 = \frac{\lambda_{\text{obs}}}{\lambda_{\text{c}}} \frac{\lambda_{\text{c}}}{\lambda_{\text{rest}}} \frac{\lambda_{\text{rest}}}{\lambda_{\text{em}}} = (1 + z_H)(1 + z_D)(1 + z_g), \tag{15}$$

where z_H, z_D and z_g denote the cosmological, Doppler and gravitational redshifts, and λ_c denotes the observed wavelength of a moving body. Hence, decoupling redshifts can be done by factorization.

2.2.2   Redshift space

Since z is a measure of the stretching of a wavelength emitted by a body, we can assume that the apparent velocity of a measured body, the Hubble flow and/or its own peculiar velocity, can be related to redshift as

$$cz = v. \tag{16}$$

If the body is only moving due to Hubble expansion, we can derive the distance to it as

$$r = \frac{cz_H}{H}. \tag{17}$$

Using our knowledge about decoupling, we may write

$$z = (1 + z_H)(1 + z_D) - 1 = z_H z_D + z_H + z_D \approx z_H + z_D, \tag{18}$$

assuming z_H and z_D are sufficiently small. Using (16) and (17), we find

$$z = \frac{rH}{c} + \frac{v_{\text{pec}}}{c}, \tag{19}$$

where we denote the movement of the observed body independent of the Hubble flow, its peculiar velocity, as v_{pec}. We have now successfully separated the two redshifts. To further capitalize on this result, we may define the redshift-space radial distance, r_z, as

$$r_z = \frac{cz}{H} = r + \frac{v_{\text{pec}}}{H}, \tag{20}$$

where H is the Hubble parameter at a given redshift. Now we are able to measure distances in redshift space (in spherical coordinates)!

2.2.3   Angular diameter distance

While we should celebrate our mathematical achievements, we note that we have yet to find out what r truly is. Thankfully, while the cosmological community has indeed not yet *built* a yardstick to measure distances, they have devised a theoretical one, taking advantage of known measures of celestial bodies. In this section, we focus on one of these devised 'yardstick' techniques.

Let us envisage a roughly spherical body hundreds of megaparsecs away, which we observe with a telescope. We can easily measure the angular diameter of the body as seen from our perspective, by angle outlined by the 'width' of the body perpendicular to our line of sight. Knowing its true diameter, the 'standard ruler', we can then exploit the trigonometry at play, calculating the angular diameter distance to the centre of the body as

$$D_A = \frac{d}{\theta}. \tag{21}$$

Before we go on, we must address the simplified image of the proper distance as defined in (5). It should be immediately clear that the constraint of a constant time is unrealistic. We note, that the light travelling from the observed body does so in a finite, but non-zero amount of time, hence the scale factor $a(t_e)$ at the time of emission did not necessarily equal that of today. We thus adjust the definition of the proper distance as

$$d_p(t_0) = c \int_{t_e}^{t_0} \frac{dt}{a(t)}. \tag{22}$$

2.2.4   Alcock-Paczyński effect

While measurements of angular diameters are, in principle, mathematically sound, in 1979 Alcock and Paczyński pointed out an additional distortion that heavily depends on the cosmological model of choice [11]. Let us come back to that spherical body we described earlier. This time, we focus our attention on the radial extent of the body along the line of sight. We notice that because the two points defining the spheres diameter lay at different points along the redshift direction, the measured light emitted from said points will be stretched to different extents. The body will hence appear elongated, appearing on the sky no longer as a sphere but as a strange cosmic egg. Which brings us to ask - if the radial extent transverse to the line of sight does not stretch similarly to the extent along said line, can we exploit this relation to measure certain cosmological parameters? First, we must find a known, almost perfectly spherical object. While, surprisingly, there are many different available choices, one holds hidden potential that may trump the currently standardized measures - *voids*.

3 VOIDS AND UNDERDENSITY

Cosmic voids are enormous regions of space that are defined primarily by their apparent relative emptiness [9]. It is easy to assume that these 'dark spots' serve only to impede our insight into the dynamics and evolutionary history of the Universe. Akin to burn-spots on old film, voids are fairly distinct from their surroundings, and yet it is that distinctiveness that inscribes voids with information seemingly inaccessible in its overdense counterparts. To understand what voids really are and how they form, we need only consider a spherical-isolated void approximation. While no individual void is perfectly spherical, and is by no means isolated, this hypothetical scenario will provide useful insight into the later inter-void dynamics. For the purposes of this thesis, we also define the underdensity as a measure of relative density composition at a given point of a void to the average background density, such that

$$\delta \equiv \frac{\rho_i}{\overline{\rho}_V} - 1 \qquad (23)$$

3.1 How do voids form?

Voids are a result of gravitationally evolved troughs in the primordial Gaussian field of density fluctuations [9], and their evolution or 'growing-up period' is largely defined by the dynamics of matter inside and around them. It is easy to fall into a misguided understanding that voids are, like other cosmic bodies, 'bodies' at all; instead, they are arbitrarily delineated regions of space, whose categorization is equivalent to that of negative space, meaning their dynamics are almost entirely described by the behaviour of matter, the positive space. Stepping away from this analogy, aside from Hubble expansion, voids grow because matter inside them is attracted to the more overdense regions around them. While this may look like the voids are 'pushing' the matter out, the voids themselves are not really doing anything. This is crucial to understanding shell-crossing.

Let us consider a homogeneously and isotropically underdense isolated spherical void, where matter can be neatly segmented into differently-sized spheres. It is easy to see that the 'pushing force' on the matter around the centre (although not literally at the centre) of the void would be the strongest, while for the outside matter layers the 'force' would be the weakest - this is because the matter from the inside of the void is attracted by the outside layers, accelerating along the radius of the void, while the outside layers are 'kept in place' by the force of the matter behind them. Because of this, the outer layers slow down, while the inner layers accelerate, effectively overtaking the outer layers in the phenomenon known as shell-crossing. The result of this action is the 'bucket' or 'top-hat' shape of the void density distribution along its radius.

It is important to note that the outgoing matter, and hence the voids themselves, initially expand with *super*Hubble flow [7]. Coming back to the definition of voids, we can now see that considering void dynamics by focusing on the matter defining them is paramount, as **voids cannot be more empty than empty!** If we think of voids as not regions of space but celestial bodies, we could naively extrapolate the superHubble flow expansion throughout time, but, as illustrated, this rate of expansion cannot last forever.

3.2 Void evolution

Individual voids, of course, are not spherical. While this is intuitively understandable, we urge the reader to consider that if voids were, in fact, isolated, they would always smooth their shapes out
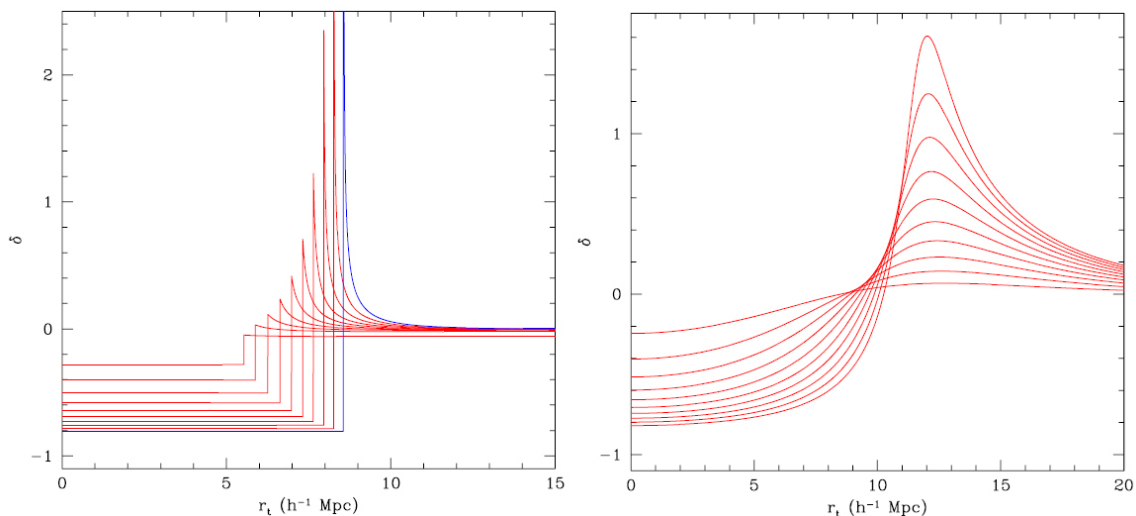
Figure 4: Spherical void evolutionary model. On the left is presented the uncompensated 'bucket' void evolving up to shell-crossing, on the right a void with an angular averaged SCDM profile. The plots clearly suggest a tendency of ridge formation with shell-crossing, as indicated by the rapidly evolved density peaks at a coinciding radial extent. From van de Weygaert [9].

to spheres. If we consider a void that has a higher overdensity along one of its principal axis, we would naturally predict that the gravitational influence on the inner mass would be stronger towards those overdensities. However, as the void expands in a preferred direction, the transverse axes start exerting a proportionally higher influence on the outgoing density, while the further-off ridges would start slowing down. This would lead to the shape of the void approximating a perfect sphere until all of its mass is gather on its borders [7][14] The result of individual voids having more ashperical shapes [15] is fascinating because it is entirely dependent on the voids' environments, and hence can shed light on the evolution of the Universe. As noted by van de Weygeart [7], we can neatly categorize two main elements of a void's evolutionary influences - interactions with other voids, i.e. merging and collapse, as well as tidal forces exerted by their environments. We first consider the latter.

3.2.1   Tidal forces

If we consider, following the suggestion by Icke [14], homogeneous ellipsoidal voids. The homogeneous aspect of the model, while by no means perfect, is a fair approximation of development of the interior of voids [7]. As should be clear from previous sections, the expanding volumes of voids are paired up with the continuous 'pull' on the matter in their interior, resulting in the 'bucket' density profile describe before. While this does break down on the edges of voids, the interior shapes are what we are interested in [7].

Considering a triaxially-symmetric homogeneous ellispoidal void, we can focus on the influence of the tidal forces exerted by the void's surroundings by following the growth of its principal axes. Indeed, van de Weygeart [7] finds that the scale-factors $\mathcal{R}_m$ due the the gravitational acceleration along the principal axes can be described as

$$\frac{d^2\mathcal{R}_m}{dt^2} = -4\pi G\rho_u(t)\left[\frac{1+\delta}{3} + \frac{1}{2}(\alpha_m - \frac{2}{3})\delta\right]\mathcal{R}_m - \tau_m\mathcal{R}_m + \Lambda\mathcal{R}_m, [7] \qquad (24)$$

denoting the background density as ρ_u and the void's underdensity as δ, while the α_m factor specifies the ellipsoidal coefficients as follows

$$\alpha_m(t) = \mathcal{R}_1(t)\mathcal{R}_2(t)\mathcal{R}_3(t) \int_0^\infty \frac{d\lambda}{(\mathcal{R}_m^2(t)+\lambda)\prod_{n=1}^3(\mathcal{R}_n^2(t)+\lambda)^{\frac{1}{2}}}.[7] \tag{25}$$

We also note the influence of the cosmological constant Λ. While seemingly daunting, focusing on specific parts of the equations rather than the whole can tell us a lot about the evolution of the voids' interior. The factor τ_m denotes the eigenvalue of the tidal shear tensor $T_{mn}^{(\text{ext})}$, and it is the primary mode in which the large-scale external tidal forces exert their influence. Looking at equation (24), we can describe the evolution of voids by three main influences - dark energy, tidal forces and internal gravitational dependencies based on the void's undersdensity. As noted by van de Weygeart, we can infer that "as δ grows strongly nonlinear, the relative influence of the large-scale (near-)linear tidal field will decline" [7]. Consequently, the more 'shallow' the void is, the more susceptible it is to the influence of external tidal fields. As pointed out before, however, voids can never exceed $|\delta| = 1$, hence the influence of tidal forces is an ever-present one.

3.2.2   Merging and collapse

In one, admittedly extreme scenario, we can imagine the tidal forces on a small, initially spherical void. As the strength of the tidal field overwhelms the expansion, it induces a preferred direction of the void's growth. The matter inside the void gets pulled along a given axis, leading to a total collapse of the 'structure'.

However, in the life of a void, tidal forces are the least of its problems. For a void to 'stay alive' as it is, it has to compete with its ever-evolving neighbours. We can imagine, for example, a small void surrounded by huge, expanding voids that start encroaching onto the small void's space. Unfortunately, to the demise of the small void, the induced squeeze by the overwhelming great regions of emptiness lead to its sad and premature death. To see the opposite side of the coin, we only need to follow-through on our example. We now imagine the remaining large voids pushing into each other. As the matter-boundaries meet, the outwards-directed velocities falter, leading to an increase in the transverse velocity component. Like foam between two coinciding bubbles, the separation fades with time, creating a new, larger void [7].

3.3   Redshift space and voids

As previously hinted at in 2.2.4, voids can become distorted due to the peculiarities inherent to redshift space measurements. While the average stacked void is a different story, the individual voids as seen on the sky are subject to a number of distortions that influence their apparent shape and contents, hence hindering our ability to identify them fairly. As noted by Ryden [16], as the Hubble parameter changes with time, the void appears stretched on the sky. This is not all however, as the contribution from the Hubble flow is minute at low redshifts, where the influence of peculiar velocities of the boundary matter dominates [16]. Finally, there are the fingers of god, which are appropriately named as they can spell doom to small voids, as well as generally decrease the size of voids. These 'fingers' come from the peculiar distortion of virialized clusters at nested in-between voids at their common boundaries. We can see the effect of the fingers of god visualised for a density map, illustrating how they quite literally poke into voids. Overall, however, we would expect the average void size to increase [16], as the voids not only stretch but so do the boundaries between them. With the addition of destruction of smaller voids by the distorted walls and fingers of god, we would then

expect to identify less voids, with more of them leaning on the larger side. This is also convincingly demonstrated by Ryden in Figure 6.
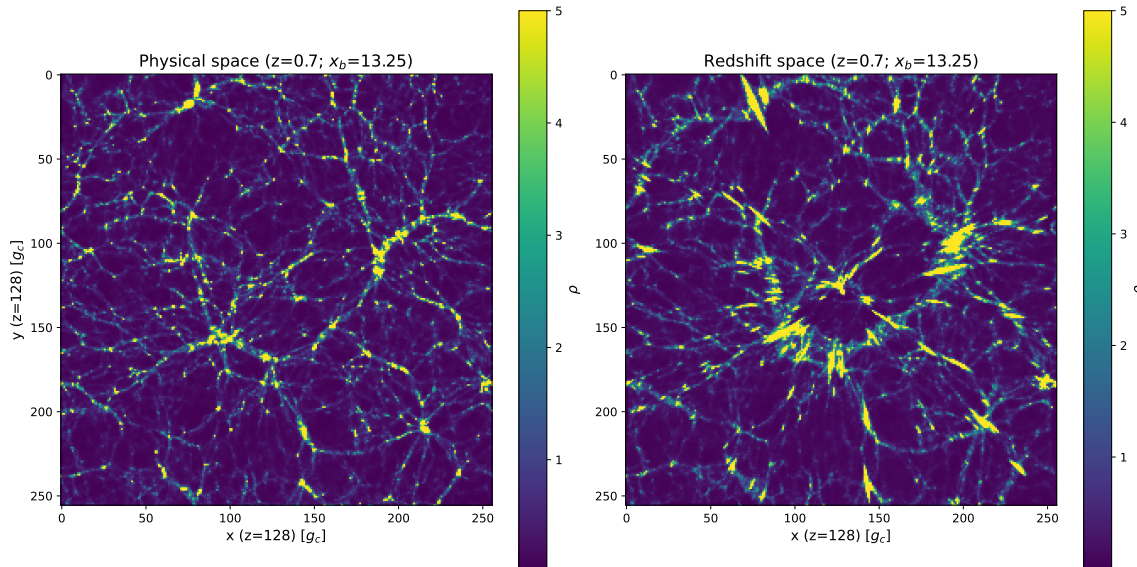

Figure 5: DTFE density maps the particle distribution of the 106.5^3Mpch^{-1} box, sliced from the middle of the z-axis, and centred at the observer position $x_b = 13.25$Mpch^{-1}. On the left, the maps is computed in physical space, showing a lack of distortions. On the right, the map is in redshift space, accurately distorted by Hubble expansion and peculiar velocities. The fingers of god point towards the centre.
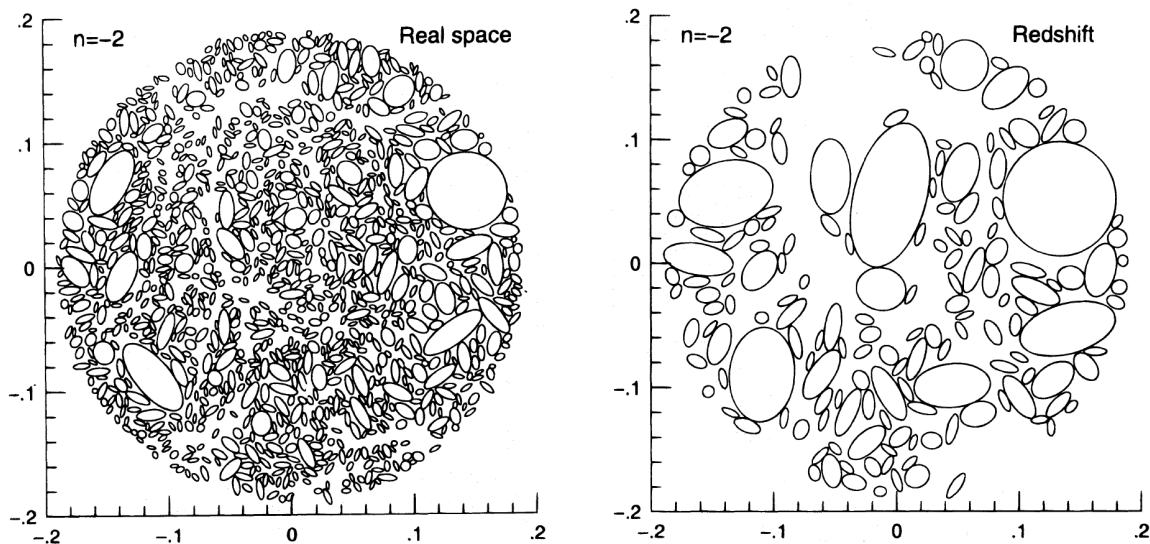

Figure 6: Identified largest underdense voids in a 2-dimensional simulation. On the left, the voids are identified in physical space. We can clearly see the abundance of small voids filling up different regions. On the right, the redshift space voids are identified to be overall larger, losing a lot of the small voids in the process. From Ryden [16].

3.4   Voids as a standard measure

As we have now explored, the lifetime of a void is filled with a myriad of different influences from without and within, molding it to fit its environment, which subsequently shapes neighbouring voids as well. It may come as a surprise then, that this chaos may be a boon rather than a vice in the context of cosmological measurements. Indeed, the overarching 'environment' of voids, as mentioned in 2, is homogeneous and isotropic, following the cosmological principle. We can then imagine, defining a void's *orientation* as the preferred direction in which it expands due to external forces, that as matter is spread out evenly throughout the universe, that voids reflect this quality by exhibiting a random distribution of orientations. The logical extension of this suggestion is that the average stacked void, that is, the void constructed by stacking all given voids around a common centre, given the same rough volume and depth, would be perfectly spherical. Of course, on its own this 'stacked void' is not very useful, however, as suggested by Ryden in 1995 [1], tracking the distortion of this artificial construction might be key to setting the standard measurement for the Alock-Paczyński test. Indeed, we would expect the stacked void to unevenly stretch *exclusively* in the redshift direction, providing a perfect probe for the investigation of cosmological parameters. Before we test this idea however, me must first fully explore the assumptions and implications of the Alcock-Paczyński test.

4   ALCOCK-PACZYŃSKI AND ELLIPSOIDS

Let us imagine a perfectly spherical void with radius $r_v(t)$, positioned very far away from some observer. We find that light coming from the centre of the void corresponds to a redshift z, while the light coming from the void's walls along the line of sight are redshifted by $z \pm \Delta z$. Following the formula for decoupling redshifts, we find

$$1 + z_{\text{tot}} = (1+z)(1+z_D) \approx (1+z)\left(1 + \frac{u_v}{c}\right) = 1 + z + (1+z)\frac{u_v}{c}, \tag{26}$$

with the fair assumption that $u_v \ll c$. Then, assuming the difference in redshifts between the walls and the center is negligible, we find

$$\Delta z = (1+z)\frac{u_v}{c}. \tag{27}$$

As shown in (21) we define the angular radius distance as $D_A = \frac{d_p}{2\Delta\theta}$, hence

$$\Delta\theta = \frac{r_v(t)(1+z)}{D_A}. \tag{28}$$

Using the definition for proper distance, we note that

$$D_A = c \int_0^{z_e} \frac{dz}{H(z)}. \tag{29}$$

Combining equations (27) and (28), we find

$$e_v(z) \equiv \frac{\Delta z}{z\Delta\theta} = \frac{u_v}{zc}\frac{D_A}{r_v}. \tag{30}$$

The above written derivation was first presented by Ryden [1], where she promptly notes, as discussed before, that 'voids tend to expand more rapidly than the Hubble flow', hence we define

$$u_v(t) = H(t)r_v(t)[1 + F(t)], \tag{31}$$

where the $1 + F(t)$ denotes the excess expansion. Overall then, we find

$$e_v(t) = \left[\frac{H(t)}{c}\frac{D_A(z)}{z}\right][1 + F(t)]. \tag{32}$$

Although we slightly altered the derivation for clarity, the resulting implications come from a fairly complex low-redshift approximation (see Peebles and Ryden [1][12]), yielding

$$e_v(z) \approx 1 + \frac{1+q_0}{2}z, \tag{33}$$

for $F(t) = 0$. The appropriate values for $F(t)$ are subject to a long-standing discussion highly dependent on the setting, in which the average void is set in [1]. For the sake of this investigation, we will only assume that $F(t)$ is a linear contribution for the stacked void, hence we expect to find a largely linear relationship as the one presented by Ryden.

4.1   Local isotropy

While the aforementioned derivation does involve certain approximations, the crucial question to the veracity of this method is whether voids are *locally* isotropic. As voids are primarily defined with respect to their overdense boundaries, we would expect the question of void isotropy to be highly related to the isotropy of the universe at large. While as indicated in 2, the universe is overall homogeneous and isotropic, it does not seem to exhibit the same properties at smaller scales [13]. Furthermore, we note that the focal process of the test - stacking, may in fact worsen this problem. As the definition of a void, and the specific parameters in the processes responsible for their identification are still a subject of debate, 'cutting' out spheres as voids to stack may inadvertently cut out the isotropy as well.

5   ILLUSTRIS SIMULATION

For the purposes of this research, we use data acquired from the Illustris simulation [17][18]. Due to the immense hardware requirements of the Illustris TNG simulation, we have chosen the lower resolution Illustris-3-Dark catalog, which exclusively focuses on the evolution of dark matter. The simulation consists of a periodic 'box' of side-length $L = 106.5cMpc$, containing around 10^8 dark matter particles of equal mass.

The simulation snapshots range from $z = 0$ to $z = 46.77$, replicating the evolution of the Universe from little after the Big Bang. In this paper, we focus on 10 snapshots from $z = 0$ to $z = 0.85$, in order to match previous research, which similarly analyses redshifts below $z = 1$ [1][2]. The particular cosmological parameters corresponding to the simulation are listed in Table 1.

Ω_m	0.2726
Ω_Λ	0.7274
Ω_b	0.0
h [$kms^{-1}Mpc^{-1}$]	0.704

Table 1: Specific parameters of the Illustris-3-Dark simulation [17].

It is important to note the units of the particle data, in particular the positions and velocities, are somewhat confusingly listed as $[ckpch^{-1}]$ and $[km\sqrt{a}s^{-1}]$, respectively. Of particular importance is the h^{-1} factor in the position units, which does not influence the stored values, and is only listed as an indicator of what one should do to get the desired units of co-moving kilo-parsecs. To obtain the peculiar velocities in co-moving coordinates, it is only necessary to divide the values by $\sqrt{a}$ (see Appendix 9.2).
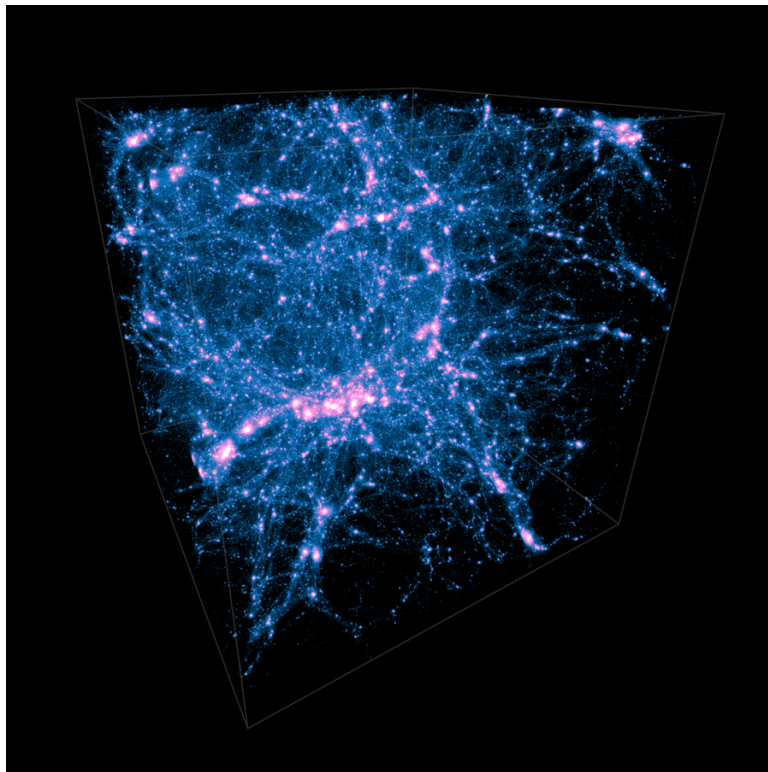

Figure 7: Illustris simulation high-resolution dark-matter particle distribution at $z = 0$. From [17].

5.1   Resolution and preliminary analysis

As described before, the aforementioned simulation of choice is of low resolution compared to the alternatives. This generally translates to a lower number of dark-matter particles, in our case 455^3. For comparison, the Illustris-1-Dark simulation contains about 1820^3, and hence is much better suited for detailed topological considerations.

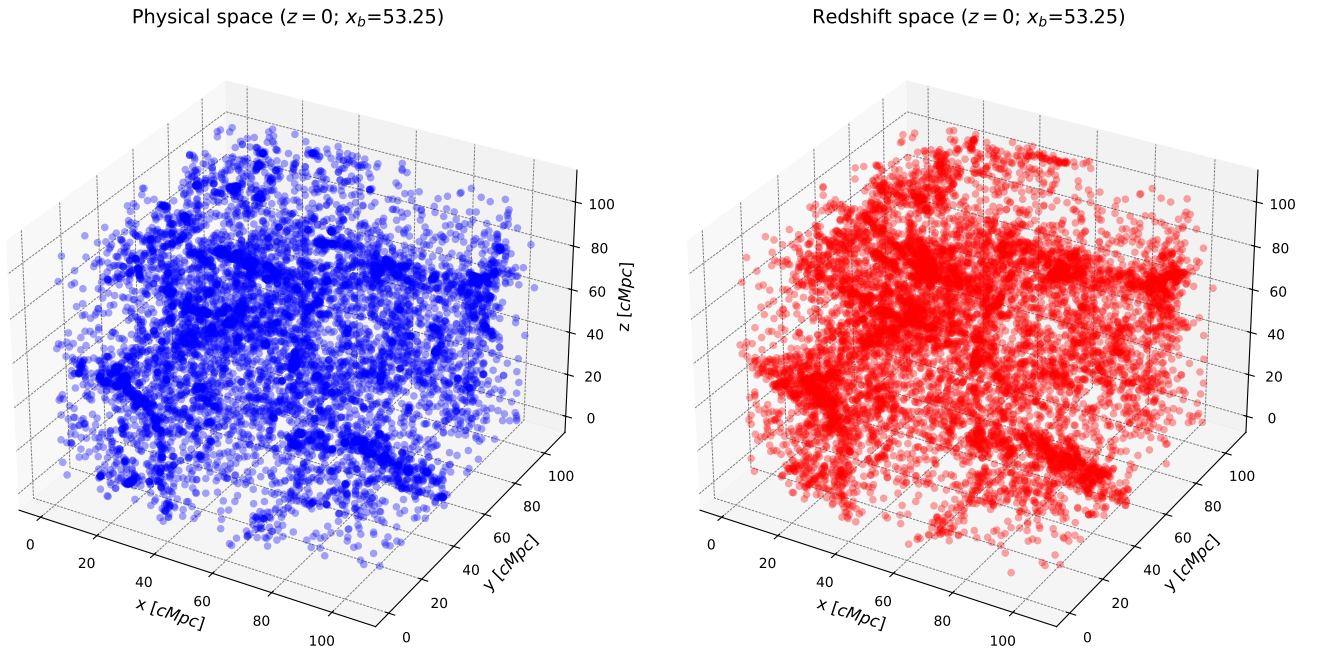Physical space ($z = 0$; x_b=53.25)   Redshift space ($z = 0$; x_b=53.25)

Figure 8: Illustris-3-Dark dark-matter particle distributions at $z = 0$, centered at $x_b = 53.25\text{Mpc}h^{-1}$, down-sampled to 0.01%. On the left, the particles are positioned in physical space, with matter clumped only in certain regions like filaments. On the right, in redshift space, matter is clearly more densely packed in regions corresponding the aforementioned filaments.

While difficult to notice, we can see a semblance of structure in both physical and redshift space raw-data plots. It is clear however, that the low resolution of the simulation will not assist us when it comes to the sheer number of particles on display - 455^3 particles is still overwhelming for non-state-of-the-art computers! To properly identify voids then, we need to utilise down-sampling tools that preserve structure, minding both the shapes and hierarchies of voids based on a chosen property - in our case, the density ratio. To do this, we introduce tessellation techniques.

6   VOID IDENTIFICATION

As explained in 5, the chosen dark-matter simulation contains an overwhelming number of particles, making it difficult to compute the necessary analysis. For this reason, we 'down-scale' the box by density interpolation. Since all the particles have the same mass, calculating the density per a specified region of the box, or 'cell', is simple, as it only requires the knowledge of the number of particles present. However, computing a full continuous map of such cells requires a relatively complex algorithm - for this, we use tessellation field estimators.

6.1   Delaunay and Voronoi tessellation

The subject of continuity is crucial when considering field reconstructions through linear interpolation. While it is simple to divide the given particle distribution into bins, the division leaves discontinuities which fail to accurately reproduce the true field, especially on a local level. Instead, Delaunay and Voronoi tessellations can be employed to estimate the field values by exploiting the geometrical properties of simple shapes. Delaunay tessellation, in 3 dimensions, focuses on dividing a given space into simple tetrahedrons, the vertices of which are located at four different points defined by the particles distribution. Subsequently, a circumsphere can be drawn onto the tetrahedron, such that the four data points are unique [19]. On the other hand, Voronoi tessellation divides the total volume of a space into unique polyhedral shapes defined by the relationship between the nucleus - data point - and the distance to other nuclei. The space defined by being closer to a specific nucleus than any other shapes the Voronoi cell. As succinctly put by Schaap and van de Weygaert, the two tessellation are "intimately related, being each others dual in that the centre of each Delaunay tetrahedron's circumsphere is a vertex of the Voronoi cells of each of the four defining points, and conversely each Voronoi cell nucleus a Delaunay vertex." [19]
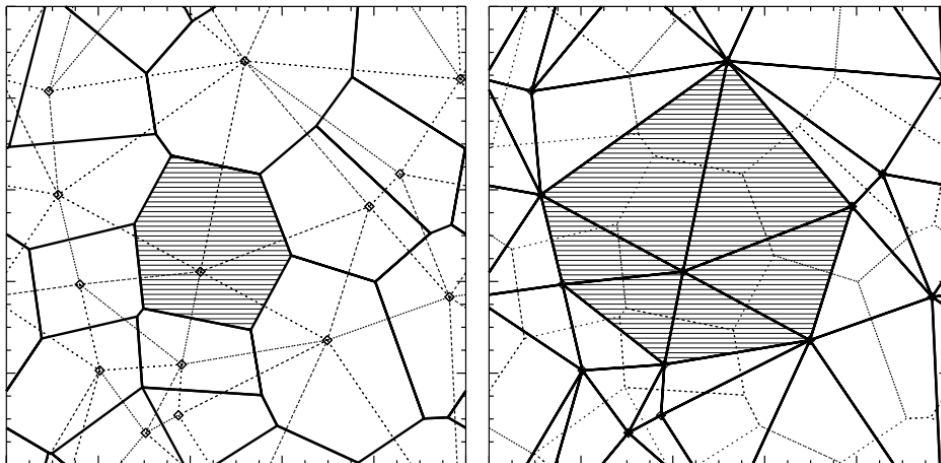
Figure 9: On the left we see the set of 20 points with their Voronoi tessellations indicated by solid lines. The shaded regions correspond to the Voronoi cell of the particle located below the centre. On the right we see the same points with their Delaunay tessellations, similarly indicated with solid lines. The shaded regions correspond to the contiguous Voronoi cell of of the same point as indicated on the left. From Schaap [19].

Following this method, we can find, for Delaunay cell vertices $\mathbf{x}_0, \mathbf{x}_1, \ldots, \mathbf{x}_M$, for an M-dimensional space spanning N particles, the linear interpolation field value reads as

$$f(\mathbf{x}) = f(\mathbf{x}_0) + \nabla f(\mathbf{x}_0)|_{\mathrm{Del}} \cdot (\mathbf{x} - \mathbf{x}_0), [19] \tag{34}$$

where $\nabla f(\mathbf{x}_0)|_{\mathrm{Del}}$ defines the constant field gradient within the Delaunay cell.

6.2   DTFE

The Delaunay Tesselation Field Estimator (DTFE), as devised by Schaap and van de Weygaert [19], uses the described tessellation techniques with the gives density estimate

$$\rho(\mathbf{x}_i) = \frac{m(1+M)}{W_{\mathrm{Vor},i}}, \quad [19] \tag{35}$$

where $W_{\mathrm{Vor},i}$ stands for the volume of the contiguous Voronoi cell of each data point, i, calculated as $W_{\mathrm{Vol},i} = \sum_{j=1}^{K} V_{\mathrm{Del},j}$. This is contrary to the density estimate of the VTFE interpolation method, which is based on $\rho(\mathbf{x}_i) = \frac{m}{V_{\mathrm{Vor},i}}$. However, as noted by Schaap and van de Weygaert, this leads to a discrepancy between the resulting mass from integration over the density field and the actual mass of the distribution [19]. We hence use the former density estimate and plug it into the previously described equation (35).
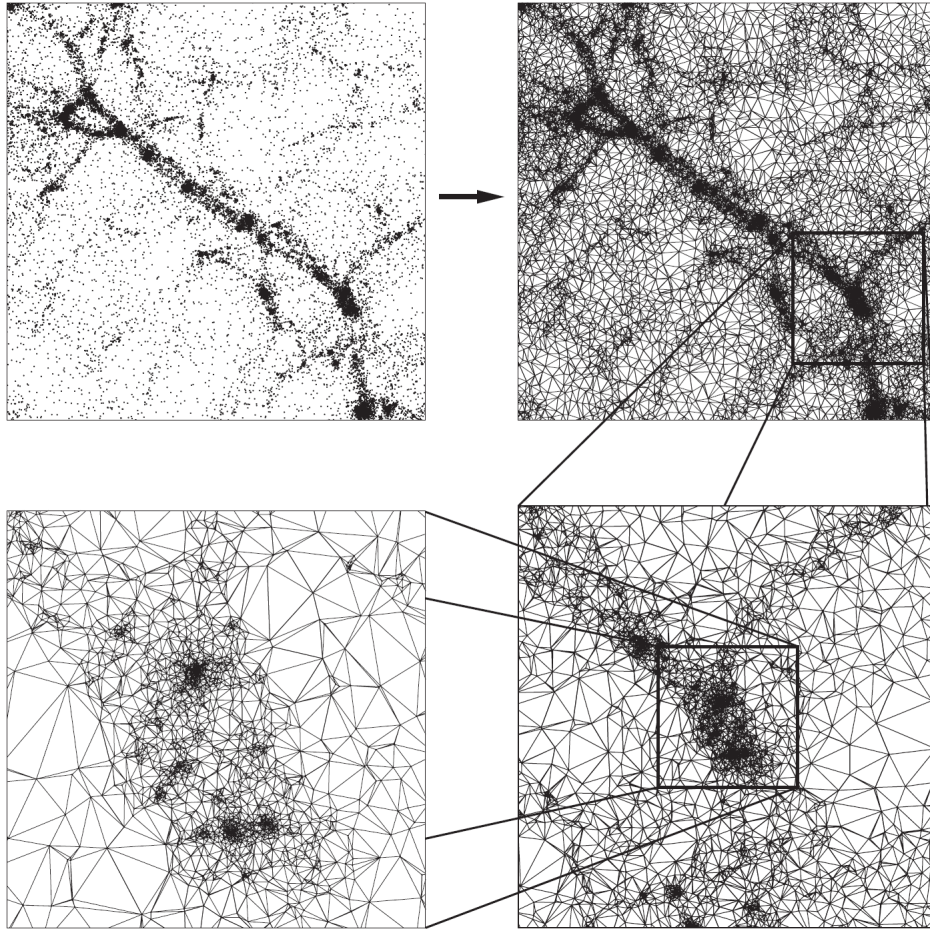

Figure 10: Delaunay tessellation of a particle distribution around a filament. The tessellation is shown at 3 different 'zoom-ins', illustrating the adaptive nature of DTFE. From Schaap [20].

We choose the DTFE method over alternatives like CIC or TSC due to the relative lack of 'noise' in the interpolated maps, which is necessary to obtain accurate shapes of voids - regions of space that should be underdense, not full of tiny particles. DTFE is triumphs by preserving the local structure of given density regions, allowing for accurate analysis and multi-scale identification of voids of different depths. For the purposes of this research, we use a 256^3 grid, with the output density-ratio values computed as $\rho = \frac{\rho_c}{\bar{\rho}}$.[2] As a majority of the analysis focuses on parameters with units of distance, from now on we define

$$g_c = \frac{106.5}{256}\text{cMpc},\tag{36}$$

as the grid-cell conversion factor.

The particular DTFE algorithm is publicly available on GitHub as generously provided by Marius Cautun [15], who's C++ implementation of the technique allowed us to properly make use of it within the very limited time constraints.

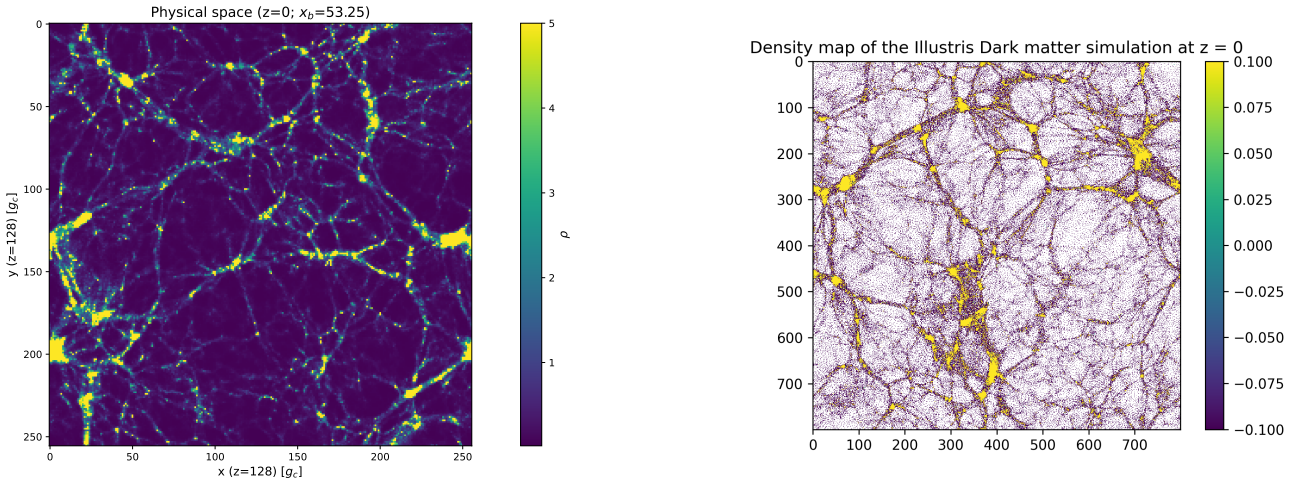

Figure 11: Comparison of the DTFE and CIC density map construction methods. On the left we see the DTFE map sliced at the middle of the z-axis, at redshift $z = 0$ and centering $x_b = 53.25 \text{Mpc} h^{-1}$. The map, although low resolution compared to existing literature, shows little noise in the distribution. On the right, the CIC map at $z = 0$ and different centering shows significantly more pronounced noise, which would inhibit the accuracy of void identification. Right image courtesy of C. Ghizdavet.

While the use of DTFE greatly simplifies the inherent complexity of a 3-dimensional particle distribution, it lacks the ability to *identify* voids. This is an issue that stems from the hierarchical nature of these regions, as described in 3. We can, naively, scan the grid for any cells with an underdensity of -0.8 or lower, but that tells us nothing about where the void begins and ends, whether the void contains smaller, deeper voids within, or whether two voids have a boundary so thin they should be merged instead. Thankfully, these questions can be answered with the considered methods - VIDE and WVF.

---

[2]From now on, when we use ρ we refer to the here defined density-ratio of the corresponding grid cells.

6.3   The watershed algorithm

How do we identify zones containing the most of 'nothing'? This question is more difficult to answer than intuition would suggest - as listed before, the hierarchical nature of voids is one of the many confounding factors presented in any potential segmentation procedure. However, in 2007, van de Weygaert, Platen and Jones utilised a clever tool commonly found in a seemingly unrelated field of geophysics - the Watershed Transform (WST) [21]. Named after the real-life concept of a drainage divide, the WST finds the minima of 'basins' - the voids - and 'floods' it with fluid, dividing the basins into domains separated by ridge-defined 'dams'. Painting a more practical picture of the algorithm, Neyrinck describes the process focusing on a single particle - WST first 'sends' the particle over to its lowest-density Voronoi neighbours. In its journey, the particle compares the lowest neighbouring cell values until it finds a minimum. The zones are defined by the set of particles moving towards the minimum, defined as the centre, or 'core', of the zone [22], like water flowing down the various ridges of a complex topological landscape.
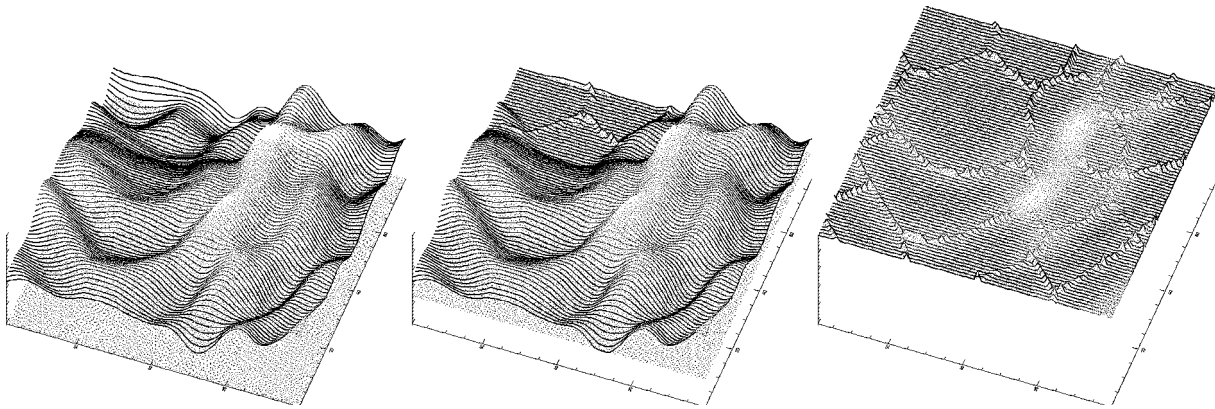

Figure 12: Illustration of the basin formation process of the watershed transform. The initial topological map is filled with 'liquid', which in time clearly separates the minima-defined regions by ridges. From Platen [21].

The watershed transform is only one of the methods used in void identification. In fact, there exist various different algorithms which choose different bases than WVF, focusing on, e.g. haloes or galaxies, as opposed to dark matter density fields. This also comes with different segmentation procedures, making for a quite varied field of inquiry. We focus on WVF as it limits the central densities of voids to those below $\delta = -0.9$, which hopefully produces a more realistic spectrum of voids. As found by Colberg *et al.*, the different methods naturally result in differences in the number and size of voids, hence comparisons to research using different methods have to account for these discrepancies [23].

6.4   VIDE

The Void Identification and Examination toolkit (VIDE) is a publicly available library comprised of different methods which allow the user to partition the void-like sectors using the Zones Bordering on Voidness (ZOBOV) algorithm, based on the VTFE density field interpolation as described in 6.1. The major advantage of VIDE is its all-in-one package approach, which helps save time and makes it easy to extract the specified data with a short set of commands belonging to the same library, written in the same computer language. However, one major drawback of the library is its reliance on the ZOBOV algorithm, which not only does not account for the integrated density field issue described in 6.1, but

also starts the identification procedure immediately, i.e. on raw data. This can lead to some loss of the hierarchical nature of the voids, mainly due to the potential of, for example, the misidentification of medium-depth voids as shallow by the inclusion of noise distortions and outliers.

6.5   WVF

Similar to ZOBOV, the Watershed Void Finder uses the WST on a density field interpolated with DTFE. However, contrary to ZOBOV, WVF contains a multitude of smoothing procedures applied before the WST. Mainly, the WVF uses natural neighbour smoothing on the DTFE input field, providing a more accurate continuous map. Additionally, the WVF reduces pixel noise before applying the WST, and introduces a hierarchy correction by removing over-segmentation of voids after the transform, the threshold for which is defined by the underdensity $\Delta = -0.8$ by default. This smoothing procedure is additionally prudent when using redshift space density fields, the spatial distortions of which can heavily influence what is identified as a void.

In our analysis, we use the WVF identification technique based on a DTFE density input. The smoothing radius for all maps is arbitrarily chosen to equal 3cMpc per cell unit length, leaving all other parameters as listed by the program by default. Although we have tried to use VIDE for additional comparison, we have found it difficult to find a way to visualize the entire VTFE map, and thus were unable to sanity-check the results.

Figure 13: WVF identified voids superimposed onto the DTFE maps, sliced in the middle of the z-axis, at $z = 0$ and centering $x_b = 53.25$Mpch^{-1}. The image on the left shows the voids identified in physical space, while the right image shows the same in redshift space. It is clear that the voids in redshift space are comparatively distorted.

Figure 14: WVF identified voids superimposed onto the DTFE maps, sliced in the middle of the z-axis, at $z = 0.58$ and centering $x_b = 53.25\text{Mpc}h^{-1}$.
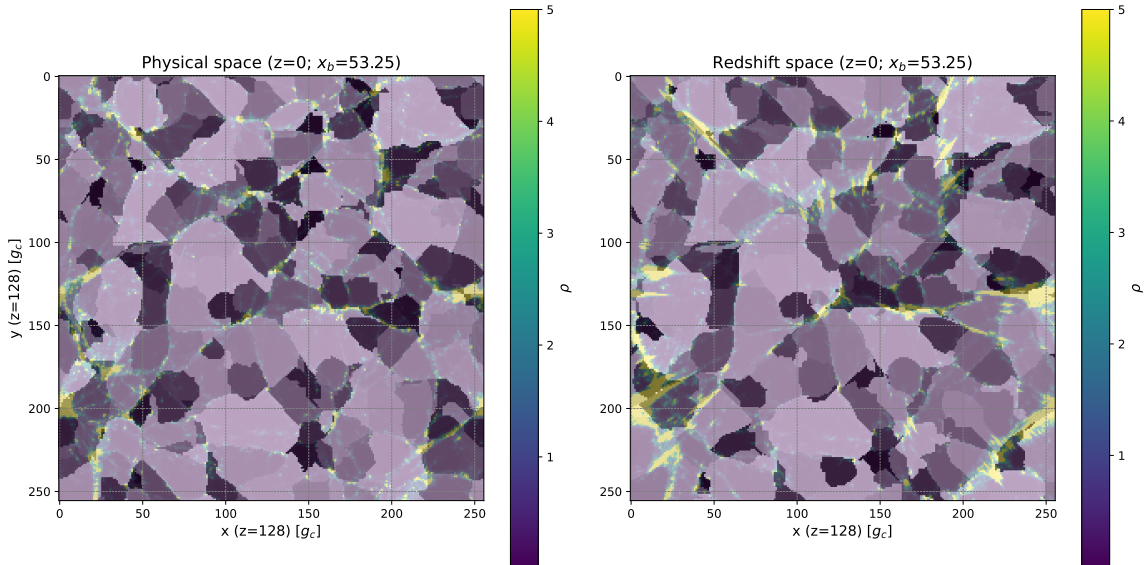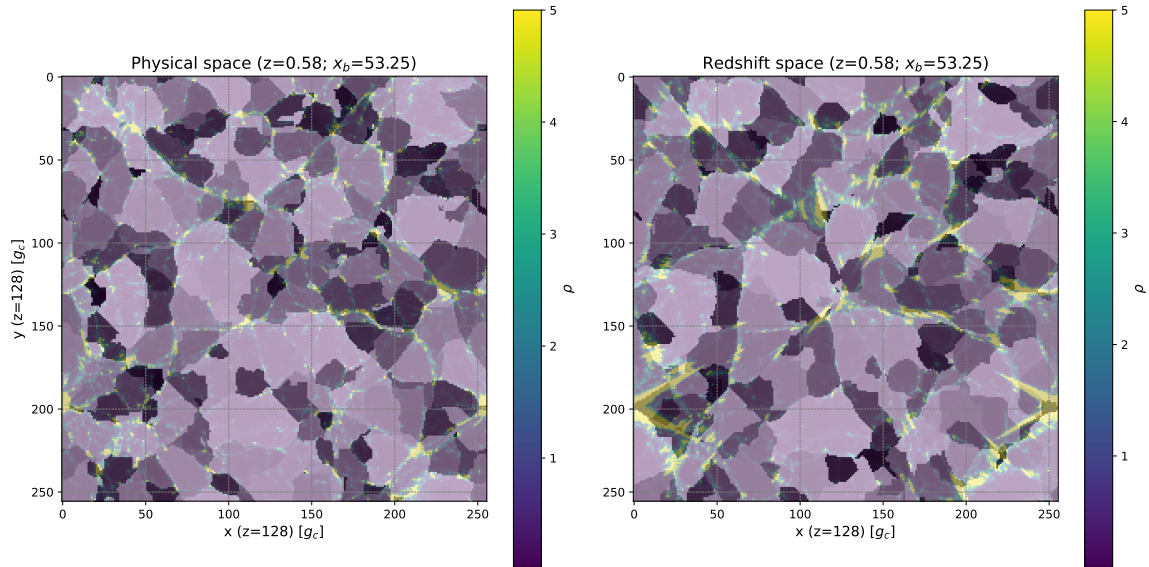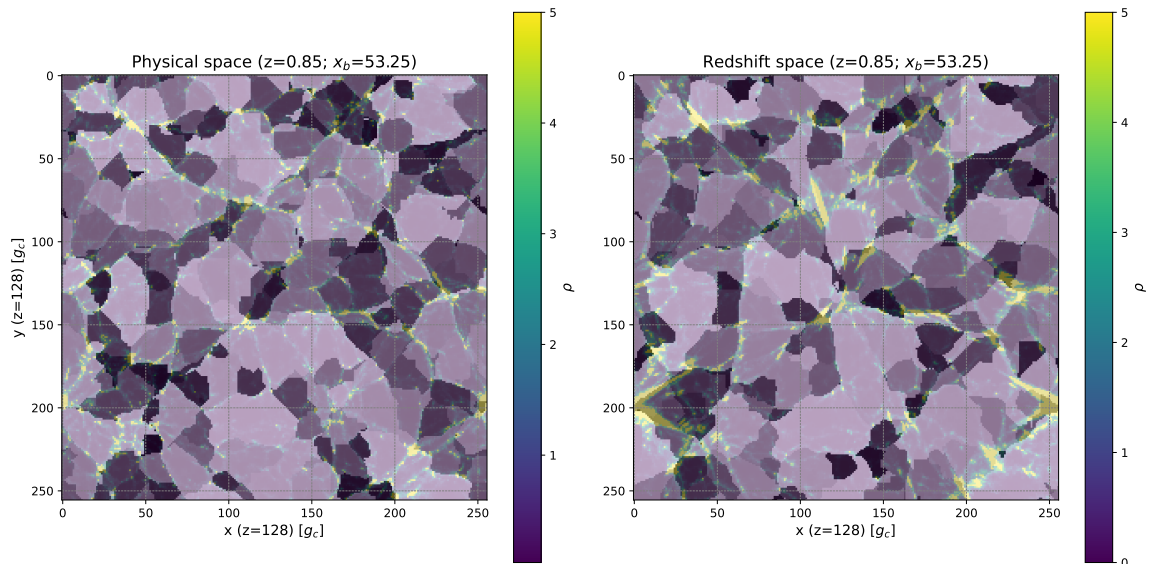

Figure 15: WVF identified voids superimposed onto the DTFE maps, sliced in the middle of the z-axis, at $z = 0.85$ and centering $x_b = 53.25\text{Mpc}h^{-1}$. With the distortion becoming more pronounced, the voids are stretched to different extents when compared with the previous figures.

7 VOID SHAPE DETERMINATION

To determine the shape of voids, we use the approximation introduced by Bos *et al.* [24], treating the voids as ellipsoids. However, we do not assume a uniform density distribution, instead opting for a less idealised result weighed by the density values corresponding to the cells contained by each basin. The approximation uses the inertia tensor of the given void particle distribution, the elements of which we define as

$$I_{ij} = \frac{1}{N} \sum_k \rho_k (\delta_{ij} \mathbf{x}_k^2 - \mathbf{x}_{ki} \mathbf{x}_{kj}), \tag{37}$$

where, as previously noted, ρ denotes the density ratio belonging to each cell, k, and N represents the total number of particles defining the basin. It is important to note the positions $\mathbf{x}_k$ are defined with respect to the void's baryocentre, which we simply define as

$$\mathbf{x}_{\text{bar}} = \frac{\rho \cdot \mathbf{x}}{\rho_{\text{tot}}}, \tag{38}$$

where $\rho_{\text{tot}} = \sum_k \rho_k$.

We then use the eigenvalues of the computed tensor to approximate the ellipsoidal semi-axes a, b, c ($a \geq b \geq c$) as follows

$$a^2 = \frac{5}{2}(I_2 + I_3 - I_1), \tag{39}$$

$$b^2 = \frac{5}{2}(I_3 + I_1 - I_2), \tag{40}$$

$$c^2 = \frac{5}{2}(I_1 + I_2 - I_3). \tag{41}$$

We define the volume of the ellipsoid as $V = \frac{4}{3}\pi r^2$,[3] where the effective radius is defined as $r = \sqrt{abc}$ [24]. Using the semi-axes, we define the ellipticity (ε), prolateness (α), and oblateness (β) of the approximated shape, such that

$$\varepsilon = 1 - \frac{c}{a}, \tag{42}$$

$$\alpha = \frac{c}{b}, \tag{43}$$

$$\beta = \frac{b}{a}. \tag{44}$$

It is easy to see how the ratios of the ellipsoidal semi-axes would illuminate our understanding of the void's sphericity. While we do assume the void to be some kind of ellipsoid, we account for the possibility of sphericity when $\varepsilon \approx 0$.

---

[3]We note the definition of volume presented in this thesis differs from the one presented in Bos' study, as we believe the additional factor of r was presented there by mistake. To check this, we point out that each semi-axis is defined in the units of [cMpc/g_c], hence the square root of their product results in a power of $\frac{3}{2}$. Accounting for this, we raise the radius to the second power.

7.0.1   Additional analysis

In order to test the accuracy of the ellipsoid-approximation method described above, we investigate the volume fraction and its relationship to redshift and observer position, which we define as

$$f_V = \frac{\sum_k V_k}{256^3}. \tag{45}$$

We expect the average volume fraction to only slightly exceed 1, as found by Bos [24]. Furthermore, we analyse the Cumulative and Probability Distribution functions (CDF and PDF) of the aforementioned parameters, as well as the relationship between ε and α for different voids.

7.1   Individual void analysis

7.1.1   Ellipticity and prolateness

We use the aforementioned methods to evaluate the voids on a non-averaged basis. This is important as it can lead us to identify potential confounding variables that might muddy later analysis. We first focus on the two main properties determining the shape of voids - the ellipticity and prolateness. We would expect a sphere to indicate $\varepsilon \approx 0$ and $\alpha \approx 1$, as naturally the ratios between the axes should be equal to 1. Instead, we find the average ellipticities $\bar{\varepsilon}$ of voids to gather around 0.56 across different redshifts and centers x_b. Interestingly, this does not seem to change in redshift space, indicating the individual voids stretch fairly isotropically without stacking.
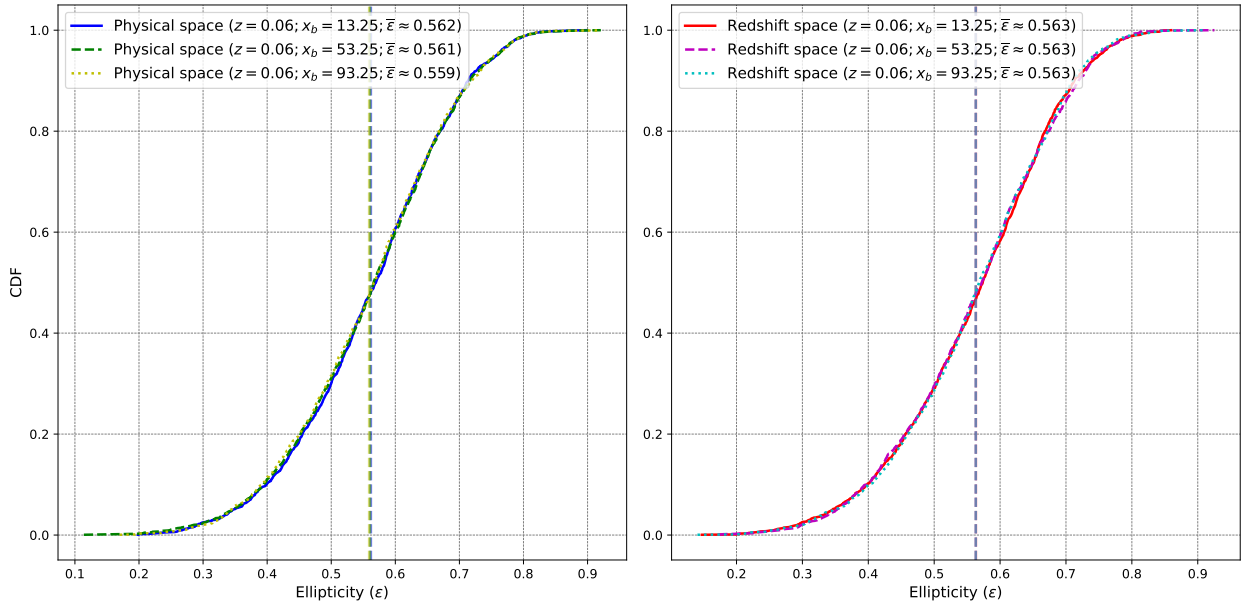

Figure 16: Comparison of CDFs of void ellipticities ε at $z = 0.06$ for different centerings, with the average $\bar{\varepsilon}$ indicated by the dotted lines. The left-hand image presents voids in physical space, while the right-hand image voids in redshift space.

This is further confirmed by CDF and PDF analysis, with the only notable changes being the peaks in the PDF values.
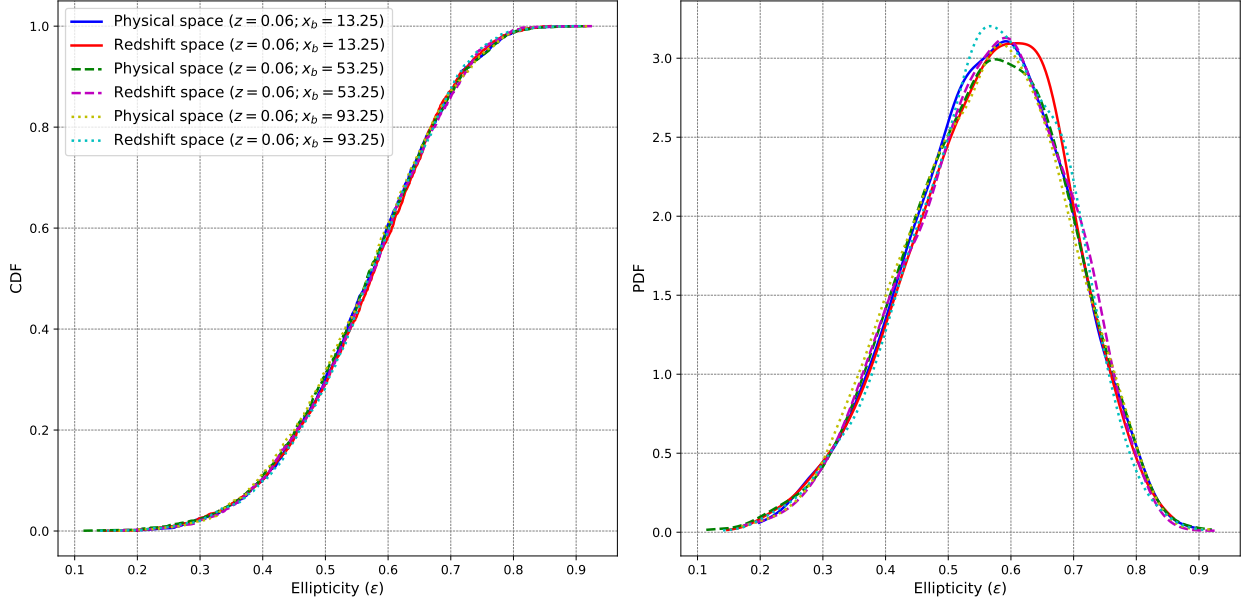

Figure 17: The CDF and PDF functions of ellipticity ε for both redshift and physical spaces at $z = 0.06$ at different centerings. While the physical distributions on the left seem to clearly coincide with their redshift counterparts, the right-hand PDF shows that this is not entirely the case. We also note that the tails of the CDFs for physical and redshift space begin at different ε values. This coincides with the results of the Kolmogorov–Smirnov test results indicated in Appendix 9.2.

We must note however, that due to the method with which we determine the ellipsoid semi-axes, that is, the requirement $a \geq b \geq c$, we cannot entirely rule out the possibility of the b semi-axis in physical space overtaking the a semi-axis in redshift space, subsequently mixing the axes' labels. We would expect this effect to be a confounding factor in situations where $\Delta(a,b) \ll 1$ in physical space. However, we note that if $a \approx b$, we would find that $\alpha \approx 1 - \varepsilon \Rightarrow s \equiv \alpha + \varepsilon \approx 1$. To check this, we focus on α CDF and PDF plots.

Looking at the average prolateness values, it is clear that they do not correspond to the aforementioned sphericity $(1 - \varepsilon)$. Indeed, across the 10 timesteps, we see that for neither physical nor redshift space does the sum of ellipticity and prolateness result in $s_i = 1$, seldom even straying from $s_i = 1.2$, indicating that the possibility of the mid-length semi-axis overtaking the longest semi-axis after conversion to redshift space is unlikely. Additionally, Tables 2 and 3 clearly show a decrease with $\bar{\varepsilon}$ with redshift. While less pronounced, this agrees with the overall trend indicated by Lee & Park [25] and Bos et al. [24].

We do note that there seems to be a higher variance in the average prolateness values in redshift space than is the case for ellipticity. This could be explained by the sheer fact that the voids are aligned, on average, in such a way that the mid-length semi-axis faces the observer moreso than its transverse counterparts. However, we would expect this to lead to elongation instead of contraction, leading to a decrease in prolateness rather than an increase. Another possibility is that this effect is due to fingers of god encroaching on the void basins in redshift space, leading to the voids' shape seemingly contracting along the b semi-axis. To answer this confusing conundrum we again turn to the relationship between ε and α. Following their definitions, with $b = $ const., we would expect an
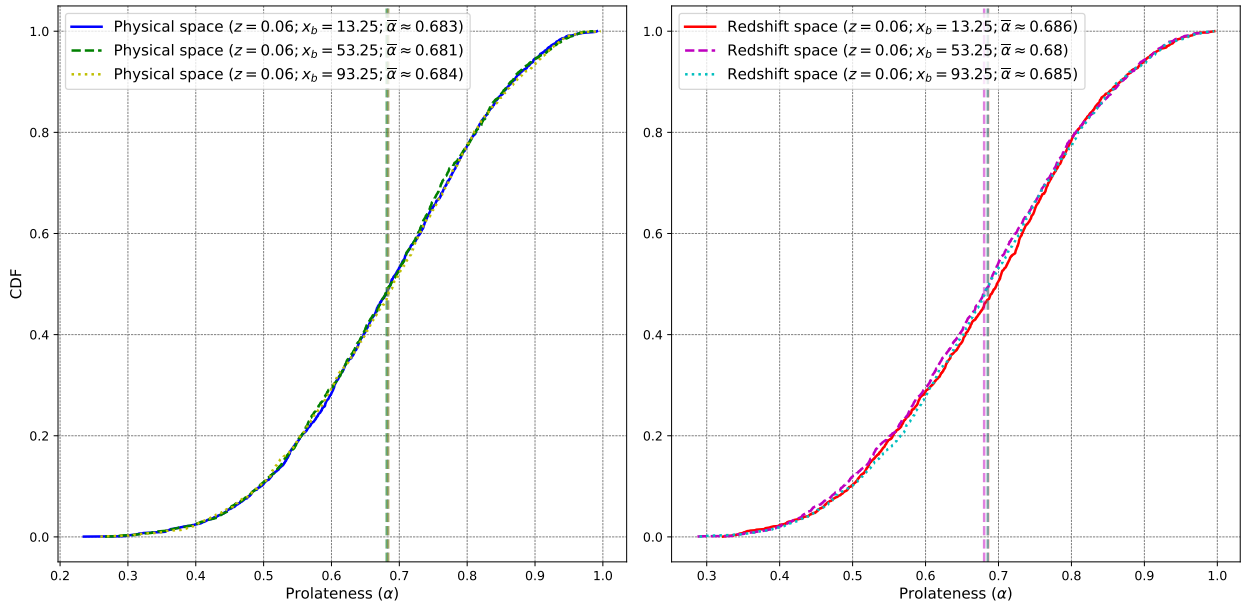
Figure 18: Comparison of CDFs of void prolateness values α at $z = 0.06$ for different centerings, with the average $\overline{\alpha}$ indicated by the dotted lines. The left-hand image presents voids in physical space, while the right-hand image voids in redshift space.
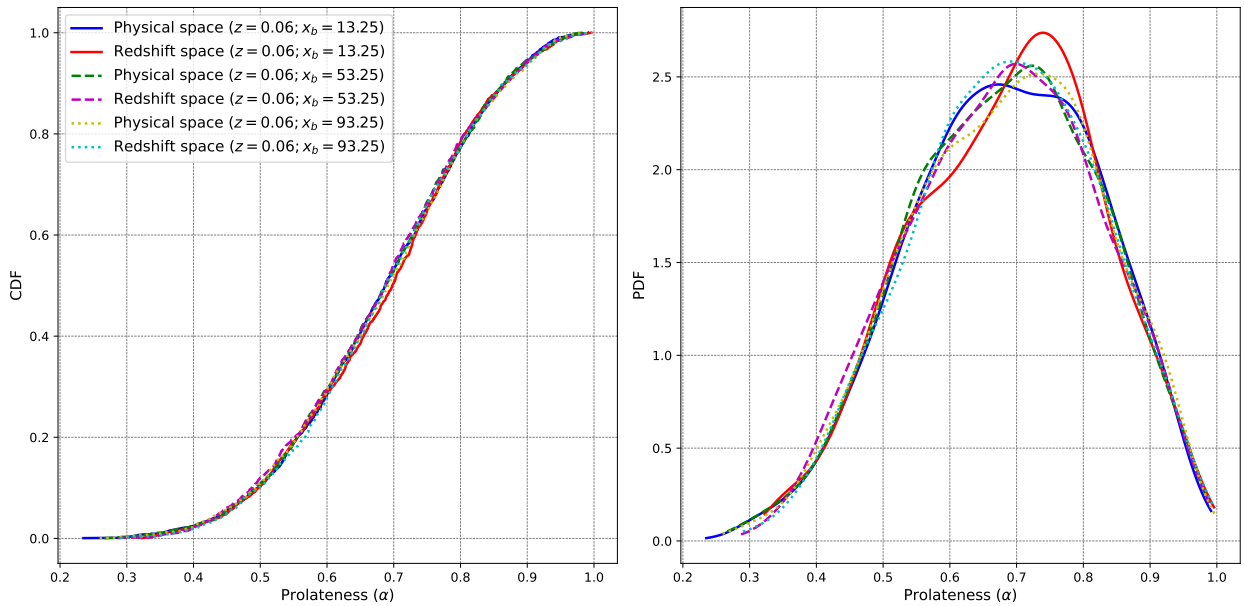
Figure 19: The CDF and PDF functions of prolateness α for both redshift and physical spaces at $z = 0.06$ at different centerings. Similarly to ellipticities, while the physical distributions on the left seem to clearly coincide with their redshift counterparts, the right-hand PDF shows that this is clearly not the case. Again, we note that the tails of the CDFs for physical and redshift space begin at different α values. This, again, coincides with the results of the Kolmogorov–Smirnov test results indicated in Appendix 9.2.

increase in prolateness to be perfectly correlated with a decrease in ellipticity. This is not the case, however, as seen in Figure 20.

$\overline{\varepsilon}; \overline{\alpha}$	x_{b1}	x_{b2}	x_{b3}	x_{b1}	x_{b2}	x_{b3}	s_1	s_2	s_3
$z = 0$	0.563	0.561	0.561	0.681	0.682	0.681	1.244	1.243	1.242
$z = 0.06$	0.562	0.561	0.559	0.683	0.681	0.684	1.245	1.242	1.243
$z = 0.13$	0.557	0.557	0.557	0.688	0.686	0.686	1.245	1.243	1.243
$z = 0.2$	0.555	0.556	0.556	0.683	0.687	0.684	1.238	1.243	1.240
$z = 0.27$	0.553	0.554	0.554	0.686	0.685	0.690	1.239	1.239	1.244
$z = 0.36$	0.549	0.551	0.549	0.692	0.690	0.692	1.241	1.241	1.241
$z = 0.46$	0.546	0.547	0.546	0.693	0.691	0.691	1.239	1.238	1.237
$z = 0.58$	0.542	0.544	0.542	0.694	0.694	0.693	1.236	1.238	1.235
$z = 0.7$	0.536	0.537	0.539	0.698	0.699	0.700	1.234	1.236	1.239
$z = 0.78$	0.533	0.531	0.530	0.702	0.703	0.707	1.235	1.234	1.237

Table 2: Table of physical space average ellipticity ($\overline{\varepsilon}$) and prolateness ($\overline{\alpha}$) values at different centerings. The sum $s_i \equiv \overline{\varepsilon} + \overline{\alpha}$ corresponds to each centering x_{bi}.

$\overline{\varepsilon}; \overline{\alpha}$	x_{b1}	x_{b2}	x_{b3}	x_{b1}	x_{b2}	x_{b3}	s_1	s_2	s_3
$z = 0$	0.565	0.563	0.563	0.684	0.681	0.685	1.249	1.244	1.248
$z = 0.06$	0.563	0.563	0.563	0.686	0.680	0.685	1.249	1.243	1.248
$z = 0.13$	0.562	0.561	0.562	0.685	0.683	0.687	1.247	1.244	1.249
$z = 0.2$	0.559	0.560	0.560	0.686	0.684	0.690	1.245	1.244	1.250
$z = 0.27$	0.557	0.558	0.559	0.686	0.685	0.691	1.243	1.243	1.250
$z = 0.36$	0.555	0.557	0.556	0.689	0.686	0.691	1.244	1.243	1.247
$z = 0.46$	0.551	0.554	0.552	0.692	0.690	0.693	1.243	1.244	1.245
$z = 0.58$	0.547	0.549	0.548	0.694	0.691	0.694	1.241	1.240	1.242
$z = 0.7$	0.543	0.545	0.546	0.696	0.695	0.699	1.239	1.240	1.245
$z = 0.78$	0.538	0.540	0.539	0.700	0.698	0.702	1.238	1.238	1.241

Table 3: Table of redshift space average ellipticity ($\overline{\varepsilon}$) and prolateness ($\overline{\alpha}$) values at different centerings. The sum $s_i \equiv \overline{\varepsilon} + \overline{\alpha}$ corresponds to each centering x_{bi}.

Regardless of centering, x_b, the relationship between ε and α is highly varied. While overall, it seems that indeed, an increase in prolateness does correlate with a decrease in ellipticity, it is overwhelmingly clear that $b \neq$ const. and hence a linear correlation function does not stand. To our surprise, this is almost exactly replicated in redshift space.

While not conclusively so due to the extremely high σ values, Figure 21 suggests a wider variance in α, seemingly confirming our suspicions about the contraction of the mid-length semi-axis. Clearly, the exact relationship between α, β and ε in voids between physical and redshift spaces is of significant interest when discussing the evolution of voids. However, due to resolution- and time-based limitations, we unfortunately leave this question open to further analysis in future research.
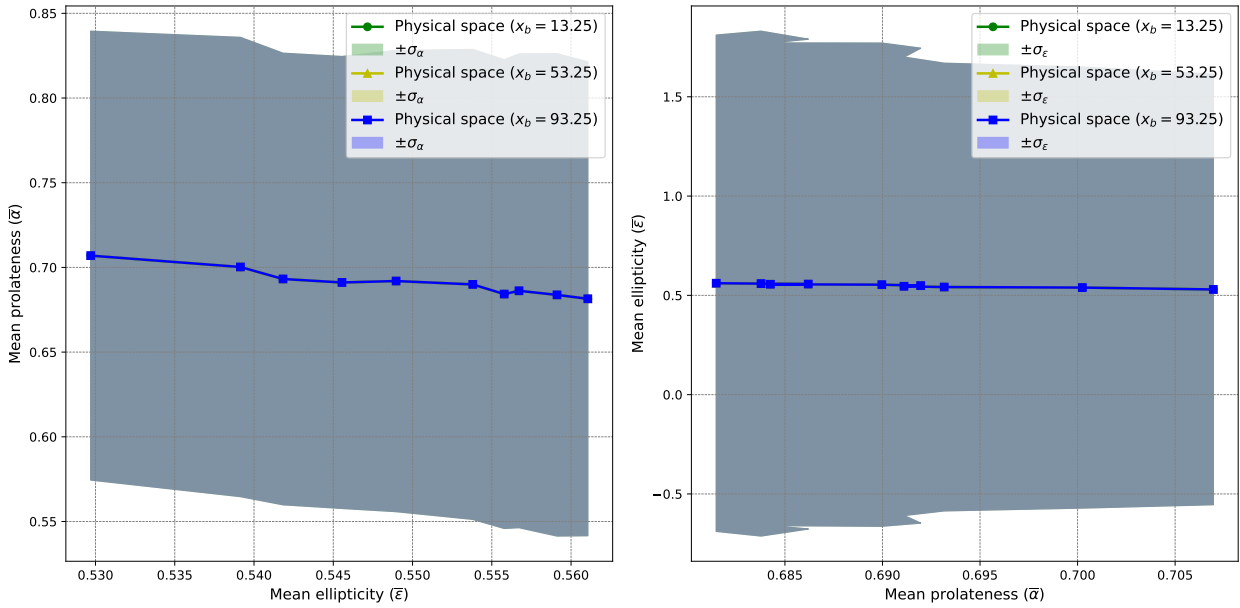
Figure 20: Average physical space ellipticity ($\bar{\varepsilon}$) and prolateness ($\bar{\alpha}$) plotted against each other at different centerings, with each point corresponding to a subsequent redshift value. The shaded areas correspond to one standard deviation σ of the corresponding y-axis variable. We note the other colours are not visible as they almost perfectly align with the other centerings.

Figure 21: Average redshift space ellipticity ($\bar{\varepsilon}$) and prolateness ($\bar{\alpha}$) plotted against each other at different centerings, with each point corresponding to a subsequent redshift value. The shaded areas correspond to one standard deviation σ of the corresponding y-axis variable. We note the other colours are not visible as they almost perfectly align with the other centerings.

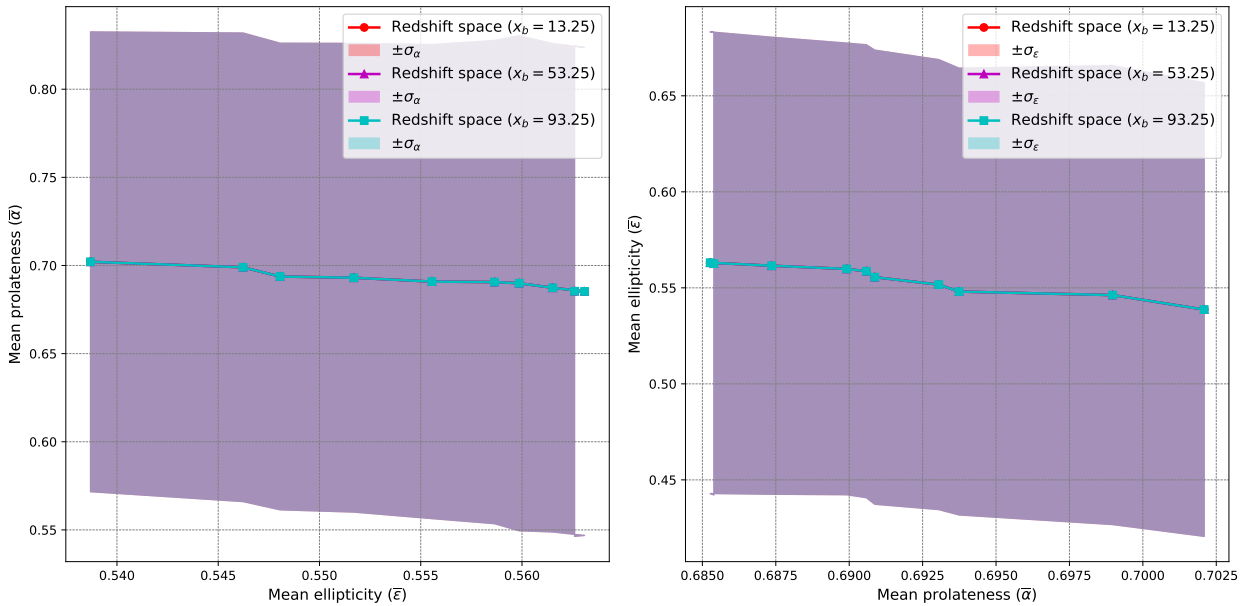### 7.1.2   Volumes

We now turn to volumes as our main indicator of the veracity of our ellipsoidal approximation. As introduced in 7.0.1, we find the volume fraction by simply dividing the sum of the interpolated volumes
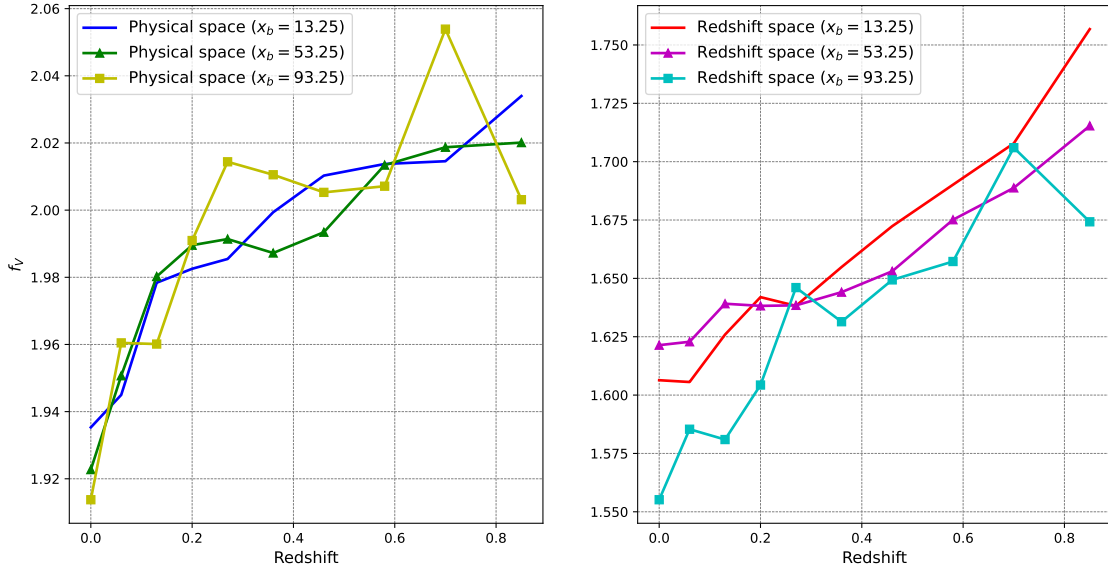
Figure 22: The evolution of volume fraction (f_V) taken up by all of the voids per centering at different redshifts. On the is outlined the physical space fraction evolution, on the right the corresponding redshift space. The volume fraction seems to consistently increase with redshift, however not enough samples are present to corroborate this conclusion.

by the total volume of the density box. As in the ellipticity analysis, we do not need to mind the units - the division takes care of them. Plotting the volume fraction, f_V, across the given timesteps, we find, to our horror, that the volumes reach up to a 2 : 1 ratio! While certainly unexpected, this result may not as catastrophic as it may first appear. As all of the properties we investigate are related to the ratios of different ellipsoidal semi-axes, the previously discussed results should be largely unaffected by this discrepancy. However, it is important to note that later analysis, focused on binning the voids by *volumes*, can be certainly called into question. If the increase is volume size is not homogeneous across all the identified voids, the voids categorized by their apparent closeness to the median volume could be unfairly mixed up. Hence, it is paramount we investigate whether the apparent increase of the voids' volumes is, or even should be, homogeneous.

To find our culprit, we look back at the inertia tensor defined in equation (37). As previously mentioned, the the tensor has a certain dependence on the density distribution in the identified voids. While we would expect this to lead to more accurate results, the approach backfires, likely to the low resolution of the chosen Illustris-3-Dark simulation. A decrease in the number of void-defining particles, resulting in a rougher density distribution, alongside the influence of overdense regions defining the void boundaries, leads to a bias in the final volumes of the voids! Indeed, as Bos et al. writes, '[b]y removing the overdense boundary regions, about 14 per cent of the volume in the voids is eliminated' [24]. This however does not coincide with the relatively low expected discrepancy ratio of 1.08 [24]. To further investigate this bias, we plot the mean parameters against the mean volume.

Unsurprisingly, in physical space, the mean ellipticity seems to be largely unaffected by the mean volume, however the same cannot be said about individual voids, due to the large σ. On the other side of the coin, the mean ellipticity seems to decrease with mean volume in redshift space, though
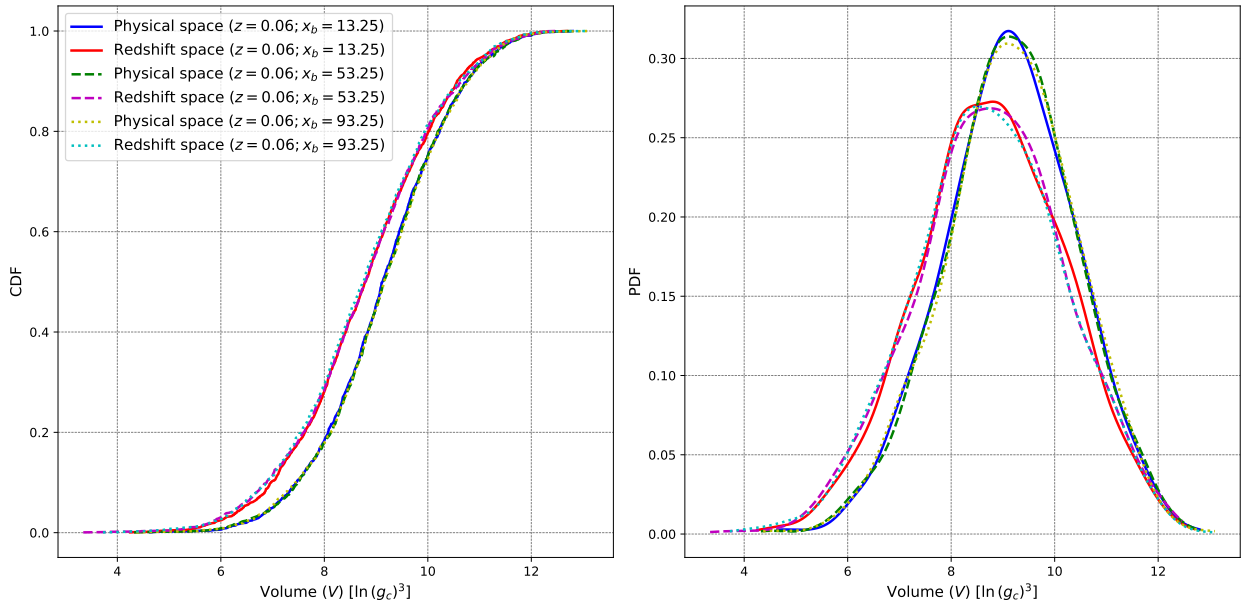
Figure 23: The CDF and PDF functions of void volume V for both redshift and physical spaces at $z = 0.06$ at different centerings. We see a clear difference between the distributions on both the left- and right-hand sides. However, we note that, in contrast to ε and α distributions, the tails of the CDFs and PDFs coincide for physical and redshift space. This may explain the counter-intuitive results of the Kolmogorov–Smirnov test results indicated in Appendix 9.2, which show an incredibly small difference and p-value. As these results are unlikely however, we take these results with high skepticism.
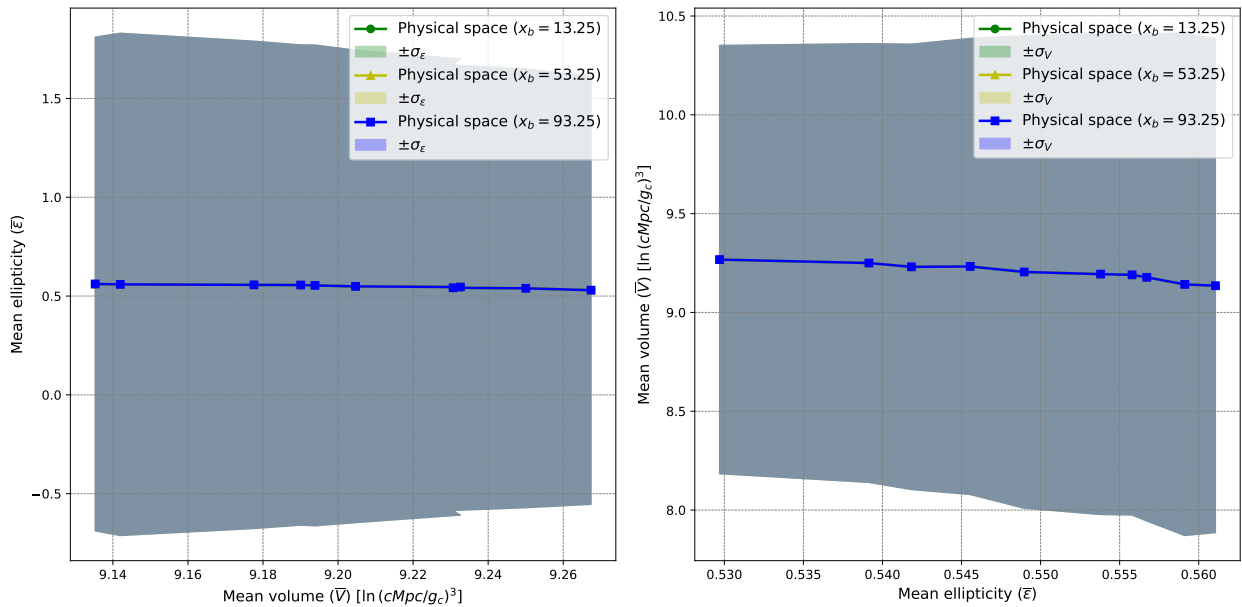
Figure 24: Average physical space ellipticity ($\overline{\varepsilon}$) and volume ($\overline{V}$) plotted against each other at different centerings, with each point corresponding to a subsequent redshift value. The shaded areas correspond to one standard deviation σ of the corresponding y-axis variable. We note the other colours are not visible as they almost perfectly align with the other centerings.

this effect is more gradual than Figure 25 would suggest, noting the logarithmic scale of the mean volume. However, these results must be taken with the full contents of a salt-shaker. Looking again at Figure 25, the two relationships are seemingly contradictory, as we would expect the mean volume to increase with mean ellipticity. This is, of course, again the result of a high σ, forcing us to accept a potential significant bias in the later stacking shape analysis.
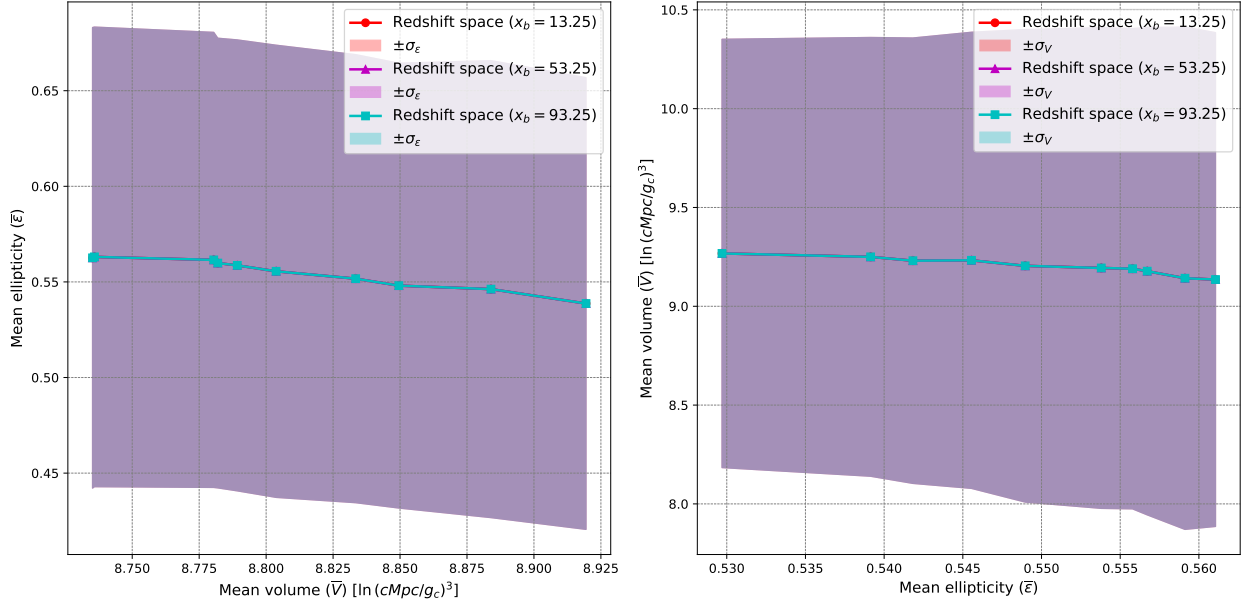

Figure 25: Average redshift space ellipticity ($\overline{\varepsilon}$) and volume ($\overline{V}$) plotted against each other at different centerings, with each point corresponding to a subsequent redshift value. The shaded areas correspond to one standard deviation σ of the corresponding y-axis variable. We note the other colours are not visible as they almost perfectly align with the other centerings.

7.2   Void stacking

We could, naively, stop the investigation of the average shape of voids on computing the average sphericity of basins at a given redshift. Indeed, the claim at the heart of the Alcock-Paczyński test is often phrased in a fairly misleading manner - from 'the average void is spherical', we refine the statement to 'the stacked void is spherical'. To paint a clear picture, we can imagine a sphere with a clearly defined circular arc with a shared centre. Indulging in this simple analogy, we rotate the arc around the sphere's centre, leaving an after-trail of differently-oriented arcs behind it. We can hence see that the sphere can be defined as an infinite 'stack' of circular arcs with a uniform distribution of orientations. Similarly, the stacked void uses this logic to create a sphere about of ellipsoids. Given voids are randomly oriented, stacking them at a common centre, while accounting for their depth and volume, should result in a sphere.

To accomplish this, we modify the clever method described by Lavaux [2] by leaving out the assumption of sphericity acted upon by taking 'spherical cuts' around each void's baryocentre. In line with Lavaux's procedure, we limit our investigation to voids of similar density, in our case - depth, and volume. Due to the limitations resulting from the relatively small sample size of this study, we provide a generous range for the volume binning, focusing on voids whose volumes lay between 30%-60% of the median volume per redshift. In contrast, we take a less favourable approach when identifying

the depth of the voids by defining deep voids as ones with more than 50% cells with values below $\delta = -0.8$, medium-depth voids as ones whose contents adhere to a 25%-50% range, and shallow voids identified below 25%. As we are only interested in the shapes of the voids, we propose the use of the ellipsoids' orientations, which we define here as

$$\mathbf{v}_o = a\mathbf{e}_a + b\mathbf{e}_b + c\mathbf{e}_c, \tag{46}$$

where $\mathbf{e}_a$, $\mathbf{e}_b$, $\mathbf{e}_c$ are the eigenvectors corresponding to the respective semi-axes. The resulting vector is unique for each void and accounts for differently directed void semi-axes. Taking the orientations of the categorized voids, we define the stacked-average void shape by the positions denoted by the orientations it is composed of, with respect to a common centre. We limit the distributions further by requiring at least 10 orientation-points per constructed ellipsoid. Finally, we assume a uniform density distribution of the stacked-average void, and calculate its ellipsoidal parameters using a modified inertia tensor from (37), where we assume $\rho_{\text{stack},k} = 1$. The resulting ellipticity should serve as a more accurate representation of the average void's sphericity.

7.3   Void stacking: results

Using the aforementioned method, we find the stacked voids for different redshifts and x_b. As an example, let us take stacks from $z = 0.27$, $x_b = 53.25$.
The first thing of note is that we cannot fulfil this requirement for shallow (S) voids. As shown in Tables 4, 5 and 6, shallow voids could not pass the sensitive restrictions, mainly lacking the required amount of orientation-points to construct a representative ellipsoid. What might be also surprising is the apparent volumes of the ellipsoids, which are *smaller* than the volume implied by the point distribution. This is likely because the parametrization of the ellipsoid involved multiplying the axes by the eigenvectors and roots of eigenvalues, resulting in a differently defined volume. However, we note that this only applies to the *plotted* ellipsoid, the implicit ellipsoid defining the void in reality follows the previously introduced definitions. Additionally, the stacked voids are highly restricted across redshifts, suggesting the lowest correlation between the chosen volume range and underdensity for the redshift of the corresponding missing values.

ε	x_{b1}	x_{b2}	x_{b3}	$\bar{\varepsilon}$
$z = 0.58$			0.532	
$z = 0.7$	0.305	0.148	0.275	0.243
$z = 0.85$	0.202	0.185	0.292	0.226
α				$\bar{\alpha}$
$z = 0.58$			0.589	
$z = 0.7$	0.785	0.916	0.889	0.863
$z = 0.85$	0.925	0.855	0.759	0.846

Table 4: Ellipticity (ε) and prolateness (α) values for stacked voids at a shallow (S) depth, with volumes between $30\% - 60\%$ of their respective median volume at a given redshift. The right-most column shows values averaged across different centerings, skipping over $z = 0.58$ due to the relative lack of results. We note that the average void shape seems to be dependent on the location of the observer.
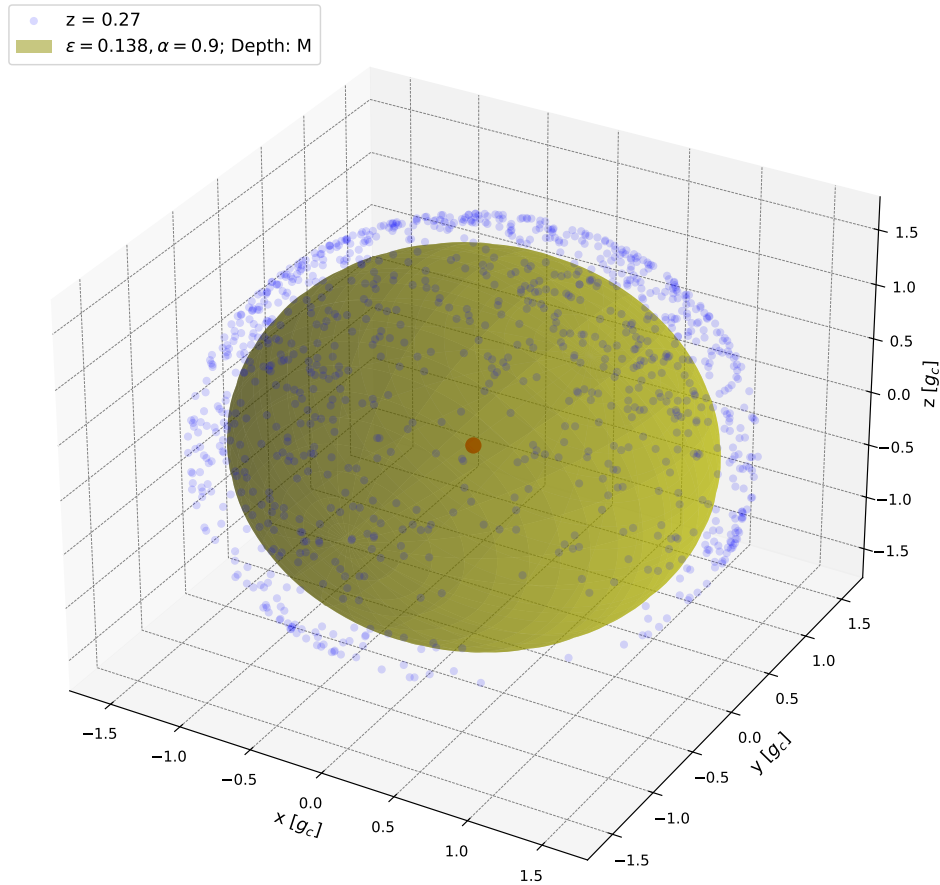
Figure 26: 3-dimensional visualization of a stacked mid-depth void in physical space, at $z = 0.27$. The defining orientation-points are indicated with blue semi-transparent dots, while the superimposed ellipsoid, centred at the red point, is indicated by a yellow surface. The drawn-on ellipsoid is smaller than the given distribution, likely because of the difference in parametrization.

Looking at the ellipticity tables, we notice that $s = \alpha + \varepsilon$, as defined for brief use in the previous sections, is closer to 1 for each stacked void than we have seen in the non-stacked mean parameters. It should also be abundantly clear that the ellipticities of the stacked voids are small, only passing 0.2 for shallow voids, which are coincidentally defined by the least orientation-points. However, it is clear that, while small, the parameters stacked voids in physical space suggest slight asphericity.

The important question now is how *almost* ellipsoidal can the stacked void in physical space be for the Alcock-Paczyński test to still properly function. While the answer to this question falls outside the scope of this research, we note that if voids do hold the potential to greatly constrict or even solve the Hubble tension, *slight* asphericities will surely hinder the confidence, with which the method is regarded by the cosmological community.
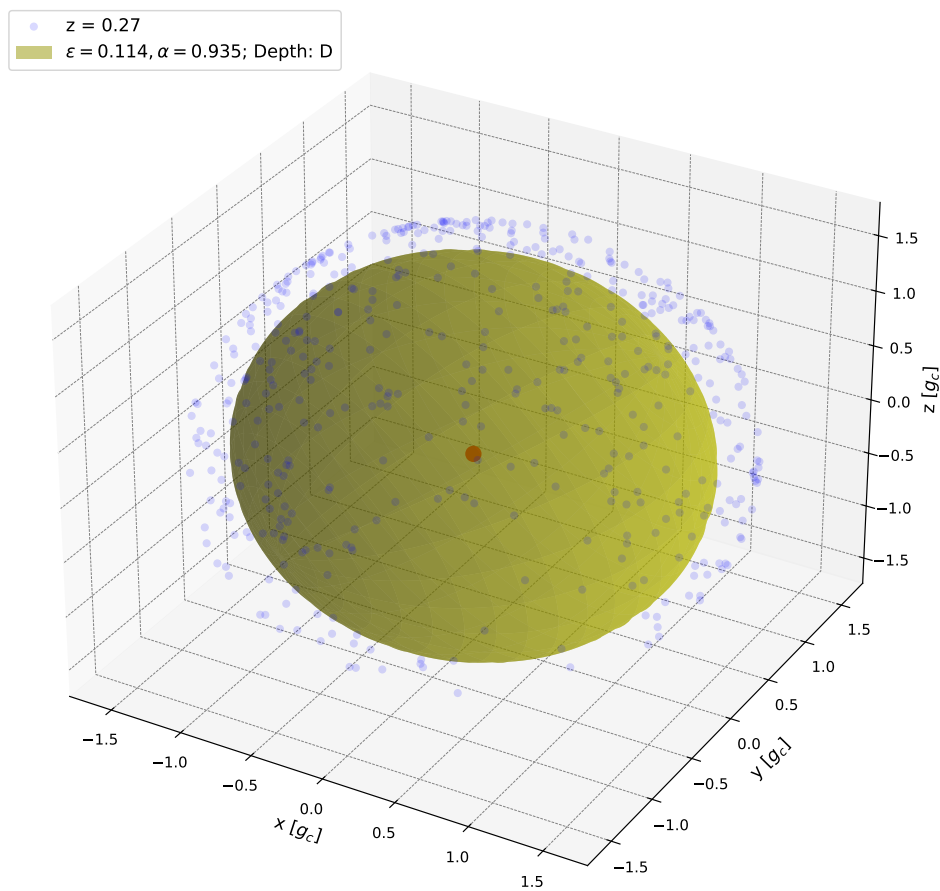
Figure 27: 3-dimensional visualization of a stacked deep void in physical space, at $z = 0.27$. The defining orientation-points are indicated with blue semi-transparent dots, while the superimposed ellipsoid, centred at the red point, is indicated by a yellow surface. Similarly, the drawn-on ellipsoid is smaller than the given distribution, likely because of the difference in parametrization.

ε	x_{b1}	x_{b2}	x_{b3}	$\bar{\varepsilon}$
$z = 0$	0.214	0.230	0.107	0.184
$z = 0.06$	0.174	0.146	0.155	0.158
$z = 0.13$	0.158	0.141	0.156	0.152
$z = 0.2$	0.165	0.134	0.152	0.150
$z = 0.27$	0.165	0.138	0.148	0.150
α				$\bar{\alpha}$
$z = 0$	0.880	0.884	0.976	0.913
$z = 0.06$	0.900	0.912	0.951	0.921
$z = 0.13$	0.904	0.914	0.919	0.912
$z = 0.2$	0.903	0.889	0.925	0.906
$z = 0.27$	0.911	0.900	0.932	0.914

Table 5: Ellipticity (ε) and prolateness (α) values for stacked voids at medium (M) depth, with volumes between $30\% - 60\%$ of their respective median volume at a given redshift. The right-most column shows values averaged across different centerings. We note the relative abundance of values compared to the shallow depth, as well as lower $\bar{\varepsilon}$ and higher $\bar{\alpha}$ values, indicating an increase in sphericity.

ε	x_{b1}	x_{b2}	x_{b3}	$\bar{\varepsilon}$
$z = 0$	0.126	0.120	0.256	0.167
$z = 0.06$	0.121	0.135	0.193	0.150
$z = 0.13$	0.116	0.124	0.170	0.137
$z = 0.2$	0.105	0.121	0.168	0.131
$z = 0.27$	0.106	0.114	0.178	0.133
α				$\bar{\alpha}$
$z = 0$	0.964	0.937	0.873	0.925
$z = 0.06$	0.929	0.921	0.872	0.907
$z = 0.13$	0.935	0.929	0.879	0.914
$z = 0.2$	0.932	0.929	0.884	0.915
$z = 0.27$	0.937	0.935	0.881	0.918

Table 6: Ellipticity (ε) and prolateness (α) values for stacked voids at deep (D) depth, with volumes between $30\% - 60\%$ of their respective median volume at a given redshift. The right-most column shows values averaged across different centerings. We again note the relative abundance of values compared to the shallow depth, as well as lower $\bar{\varepsilon}$ and higher $\bar{\alpha}$ values, indicating an increase in sphericity. The values are, however, curiously lower than their mid-depth counterparts, which begs further investigation.

8   ALCOCK-PACZYŃSKI TEST

While this thesis is mainly focused on the underlying assumption of the AP test, for which we have found contrary evidence, we indulge our curiosity by applying a modified version of the AP test to the analysed data. We note, however, that the redshift space positions of the dark matter particle distribution are computed with peculiar velocities as described in 2. This, as we have thoroughly explored, introduces a factor $F(t)$ in equation (32). While this 'peculiar distortion' can be approximated for different cosmological models, calculating it is out of the scope of our investigation. However, we can still analyse the relationship between e_v and z by noticing that the distortions due to peculiar velocities should be small for low redshifts. With this in mind, we can focus on the *shape* of the function describing $e_v(z)$ viewed by differently positioned observers.

8.1   Radial and angular extents

Similarly to the shape determination method, we bin the voids by depth and volume. It is important to note that while in 7.2 we describe the stacking process for the void *shapes*, here we are interested in a more thorough approach by stacking the void density distributions themselves. The radial and angular extents are hence weighted by the actual particles defining the stack, as is done by Lavaux [2].

As we are not assuming the average void is spherical, we must account for the possibility that the average void can be oriented at any angle relative to the line of sight. We can imagine, for example, a void which is oblate along the line of sight, matching the radial extent of an equivalent sphere, and prolate perpendicular to it. The stretching resulting from redshift distortions could create the illusion that this void is spherical in *redshift space*, leading to nonsensical e_v estimates! We hence do not 'fix' the orientation of the stacked void and define its radial extent by taking the distance to the point pierced by a line defined by

$$v_x = b \sin\left(\arccos\left(\frac{c}{\sqrt{a^2+b^2+c^2}}\right)\right)\cos\frac{\pi}{4}, \tag{47}$$

$$v_y = b \sin\left(\arccos\left(\frac{c}{\sqrt{a^2+b^2+c^2}}\right)\right)\sin\frac{\pi}{4}, \tag{48}$$

$$v_z = b \sin\left(\arccos\left(\frac{c}{\sqrt{a^2+b^2+c^2}}\right)\right), \tag{49}$$

from the stacked void's centre. The void itself being parametrized by

$$x = a\sin\theta\cos\phi, \tag{50}$$

$$y = b\sin\theta\sin\phi, \tag{51}$$

$$z = c\cos\theta, \tag{52}$$

where $0 \le \theta \le \pi$, $0 \le \phi \le 2\pi$. Similarly, for the angular radius, we first find the points pierced by the perpendicular vector

$$v'_x = a\sin\frac{\pi}{2}\cos\left(\arctan\left(-\frac{a}{b}\right)\right), \tag{53}$$

$$v'_y = b\sin\frac{\pi}{2}\sin\left(\left(\arctan-\frac{a}{b}\right)\right), \tag{54}$$

$$v'_z = c\cos\frac{\pi}{2}, \tag{55}$$

then, under the small-angle approximation, we compute

$$\Delta\theta = \frac{||\mathbf{v'}||}{128\sqrt{3}},$$

as the stacked void is centred in the middle of the 256^3 grid. However, we must note that this method is prone to significant bias. This is mainly due to the method of finding the angular radius, as the 'proper' technique would require the width of the void to be defined by tangent lines to the ellipsoid coming from the grid origin. However, this was not possible due to significant time constraints, we hence urge the reader to keep this in mind when discussing the results.

8.2   Alcock-Paczyński test: results

With the understanding that our investigation has thus far indicated asphericity of physical space stacked voids, we proceed to the results of the Alcock-Paczyński test.
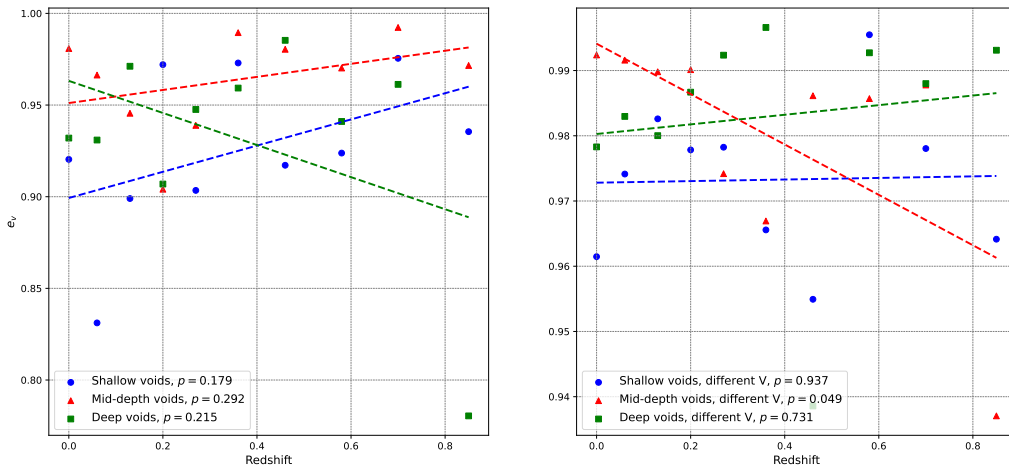

Figure 28: Plots of e_v against redshift for different stacked voids at $x_b = 13.25\text{Mpc}h^{-1}$. The left-hand image shows voids stacked by volume *and* depth, while the right hand image indicates binning by depth *only*. The imposed linear functions have p-values indicated in the legend, with most of them being above $p = 0.05$, indicating little correlation to the point distribution.

Plotting the void expansion $e_v(z)$ as a function of redshift, we find the results to be essentially nonsensical. We see the p-value of the 'forced' linear relationships rarely pass under the standard $p \leq 0.05$. We note that this seems to be consistent only for mid-depth voids binned *only* by density, although this trend seems to break at $x_b = 93.25$. This leads us to the curious dependency on the chosen centering of the particle distribution. While for all the other results the choice of x_b seemed to have no significant effect, the AP test seems to be highly allergic to the change of observer location. This, naturally, makes little sense if stacked voids are supposed to be spherical - we would expect the voids to stretch only in the radial direction, which is defined *with respect to the observer*. However, we also cannot be overconfident in the veracity of these findings. The proposed method of actually measuring the radial and angular extents is imperfect as previously mentioned. It is possible that figures 31, 32, 33, do not fairly reflect the void expansion we would find when looking at the stacked void from very far away. We hence test the method proposed by Ryden [1], where we align one of the axes with the
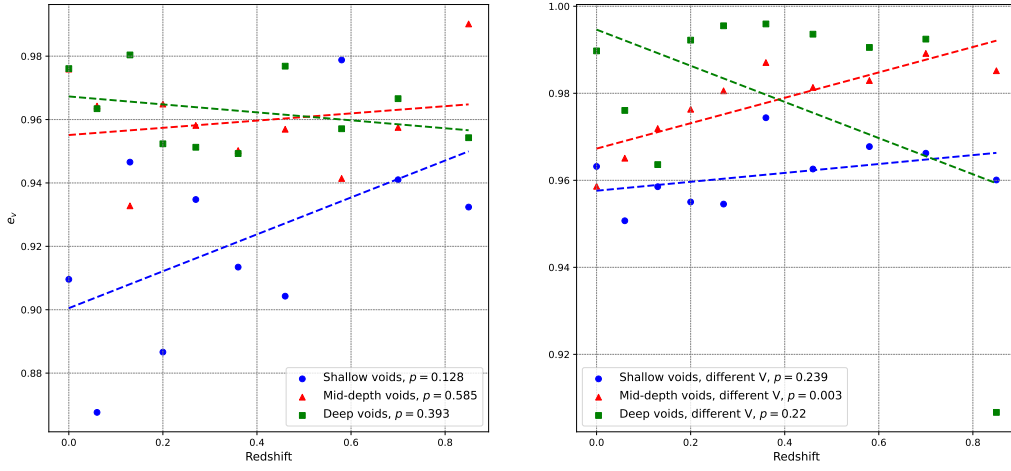
Figure 29: Plots of e_v against redshift for different stacked voids at $x_b = 53.25\text{Mpc}h^{-1}$. The left-hand image shows voids stacked by volume *and* depth, while the right hand image indicates binning by depth *only*. The imposed linear functions have p-values indicated in the legend, with most of them being above $p = 0.05$, indicating little correlation to the point distribution.

Figure 30: Plots of e_v against redshift for different stacked voids at $x_b = 93.25\text{Mpc}h^{-1}$. The left-hand image shows voids stacked by volume *and* depth, while the right hand image indicates binning by depth *only*. The imposed linear functions have p-values indicated in the legend, with most of them being above $p = 0.05$, indicating little correlation to the point distribution.
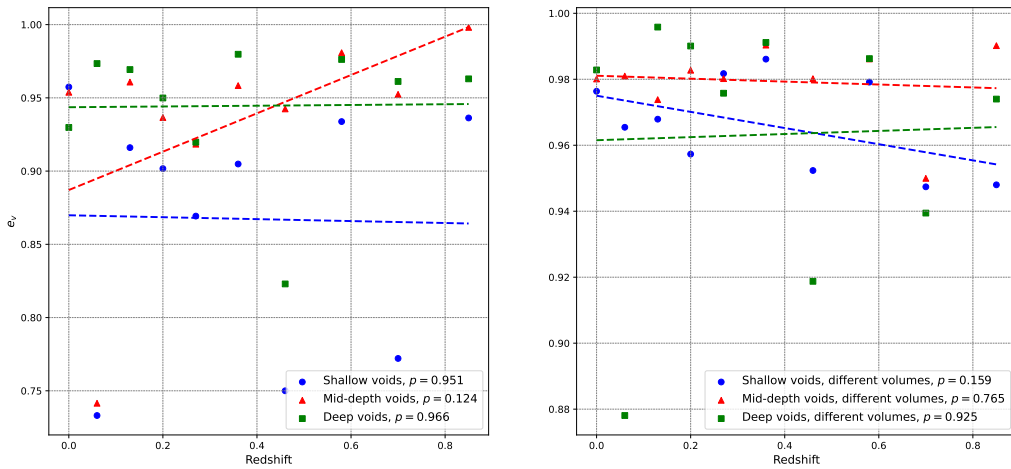
radial direction. However, because of the 3-dimensional nature of our simulation of choice, we need to choose one of the other two axes to serve as the angular extent of the void. While, naturally, for a spherical stacked void this would be of no consequence, we note that the choice of semi-axes is skewed by the imposed relationship $a \geq b \geq c$! This means that the choice of the longest semi-axis, a, might not reflect the radial stretching of the void. Nonetheless, we proceed with the test, keeping in mind these confounding factors.
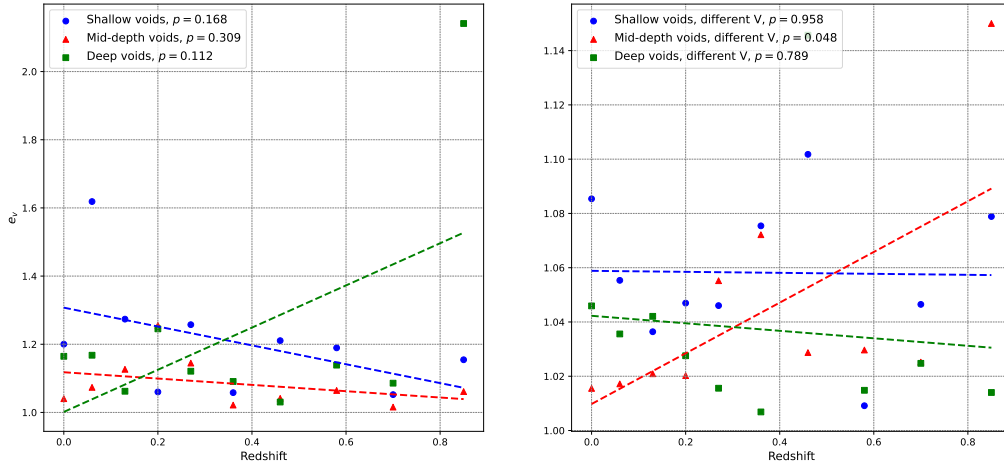
Figure 31: Plots of e_v against redshift for different stacked voids at $x_b = 13.25\mathrm{Mpc}h^{-1}$. The values stem from an adjusted method of gathering the radial and angular extents. The left-hand image shows voids stacked by volume *and* depth, while the right hand image indicates binning by depth *only*. The imposed linear functions have p-values indicated in the legend, with most of them being above $p = 0.05$, indicating little correlation to the point distribution.
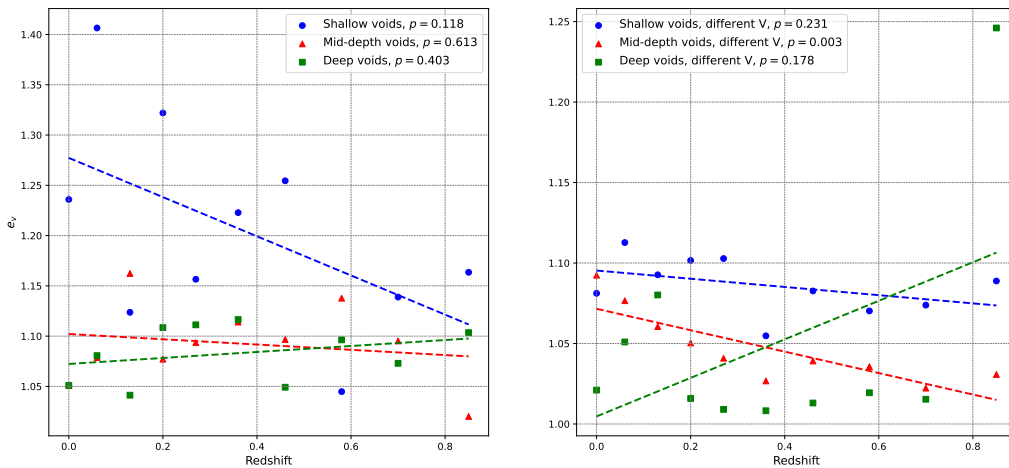
Figure 32: Plots of e_v against redshift for different stacked voids at $x_b = 53.25\mathrm{Mpc}h^{-1}$. The values stem from an adjusted method of gathering the radial and angular extents. The left-hand image shows voids stacked by volume *and* depth, while the right hand image indicates binning by depth *only*. The imposed linear functions have p-values indicated in the legend, with most of them being above $p = 0.05$, indicating little correlation to the point distribution.
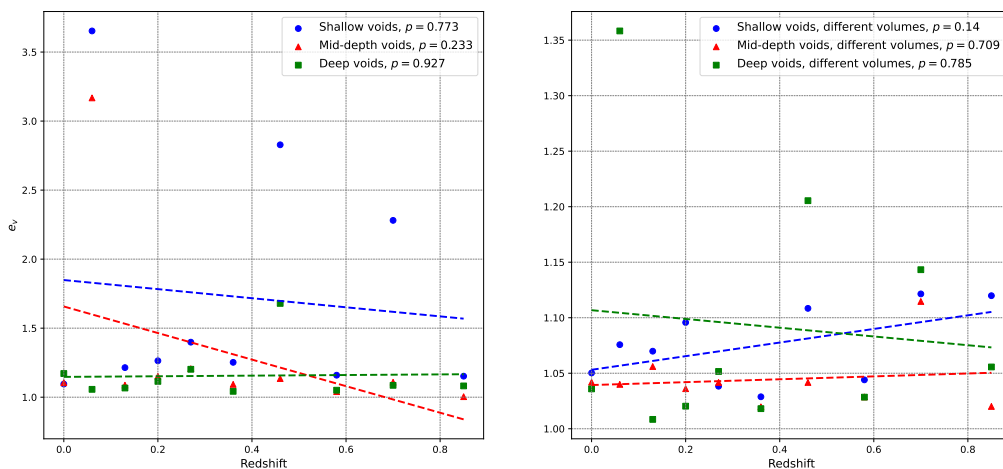
Figure 33: Plots of e_v against redshift for different stacked voids at $x_b = 93.25\text{Mpc}h^{-1}$. The values stem from an adjusted method of gathering the radial and angular extents. The left-hand image shows voids stacked by volume *and* depth, while the right hand image indicates binning by depth *only*. The imposed linear functions have p-values indicated in the legend, with most of them being above $p = 0.05$, indicating little correlation to the point distribution.

While it seems that, generally, this method produces more precise results, a linear relationship under the volume-depth constriction cannot be drawn for any observer. Again, we note that the choice of observer location should not even matter! However, we also point out that the methods, which which the AP test was performed, are highly questionable, and hence no real conclusions can be drawn other than the sheer fact that the matter requires more research.

9   CONCLUSION AND DISCUSSION

9.1   Findings

The results of our investigation are as varied as the debate surrounding them in the larger cosmological community. While we have found that the average stacked void is not *perfectly* spherical, the accuracy of our results is hindered by the limited sample we have drawn upon. Furthermore, it is clear that the inhomogeneous ellipsoidal parametrization has resulted in shape-related biases that artificially increase the volume fraction that voids constitute. As the relationship between volume and other shape-defining parameters like ellipticity and prolateness was found to contain enormous standard deviations, we cannot confidently state that this bias has not affected our results. This, of course, also translates in the uncertain results of the Alcock-Paczyński test. Both due to the methods with which $e_v(z)$ was derived, as well with which the stacked redshift void was constructed, the results of the AP test across the 10 investigated timesteps do not reflect a fair and unbiased assessment of the veracity of the spherical assumption. We do hope however, that this investigation has brought valuable insight to the cosmological table and will inspire further investigation of the presented issues.

9.2   Suggestions

We suggest a large-scale analysis of high resolution Illustris TNG data, with the use of DTFE and WVF for density tessellation and void analysis. With the study of voids in redshift space, we note that adjusting the smoothing radius with respect to the redshift may be necessary to accurately reflect the multi-scale nature of the cosmic web. Furthermore, we urge future research to take the overdense borders into account when defining the voids, and keeping the use of the inhomogeneous density-ratio inertia tensor for improved accuracy. We believe that with a higher resolution and improved multi-scale categorization, this adjusted ellipsoidal parametrization can shed more insight on a less idealised model of the stacked void, introducing a necessary bias that reflects cosmological measurement. For the derivation of the $e_v(z)$ factor, it is important that different methods of finding the radial and angular extents of the stacked voids are tested, preferably in a way that accounts for the possibility of void orientations at an angle to the line of sight. We hope to find the future research of cosmic voids to fastidiously cover its bases and checking its fundamental assumptions, leading the study of the mysteries of the universe.

Bibliography

[1] B. S. Ryden, "Measuring q 0 from the distortion of voids in redshift space," *The Astrophysical Journal*, vol. 452, p. 25, Oct. 1995.

[2] G. Lavaux and B. D. Wandelt, "Precision cosmography with stacked voids," *The Astrophysical Journal*, vol. 754, p. 109, July 2012.

[3] "The universe's building blocks." https://science.nasa.gov/universe/overview/building-blocks/#dark-matter. Accessed: 2024-07-02.

[4] J. Hidding, R. van de Weygaert, G. Vegter, and B. Jones, "Adhesion and the geometry of the cosmic web," in *The Thirteenth Marcel Grossmann Meeting: On Recent Developments in Theoretical and Experimental General Relativity, Astrophysics and Relativistic Field Theories - Proceedings of the MG13 Meeting on General Relativity (in 3 Volumes). Edited by ROSQUIST KJELL ET AL. Published by World Scientific Publishing Co. Pte. Ltd., 2015. ISBN 9789814623995, pp. 2142-2144* (K. Rosquist , R. Jantzen, and R. Ruffini, eds.), pp. 2142–2144, World Scientific Publishing, Jan. 2015. The Thirteenth Marcel Grossmann Meeting on General Relativity ; Conference date: 01-07-2012 Through 07-07-2012.

[5] W. Liu, D. Wu, X. Fang, J. Jing, and J. Wang, "Kerr-mog-(a)ds black hole and its shadow in scalar-tensor-vector gravity theory," 2024.

[6] E. Di Valentino, O. Mena, S. Pan, L. Visinelli, W. Yang, A. Melchiorri, D. F. Mota, A. G. Riess, and J. Silk, "In the realm of the hubble tension—a review of solutions *," *Classical and Quantum Gravity*, vol. 38, p. 153001, July 2021.

[7] R. van de Weygaert, "Voids and the cosmic web: cosmic depression amp; spatial complexity," *Proceedings of the International Astronomical Union*, vol. 11, p. 493–523, June 2014.

[8] S. A. Gregory and L. A. Thompson, "The Coma/A1367 supercluster and its environs.," , vol. 222, pp. 784–799, June 1978.

[9] R. van de Weygaert and E. Platen, "Cosmic voids: Structure, dynamics and galaxies," *International Journal of Modern Physics: Conference Series*, vol. 01, p. 41–66, Jan. 2011.

[10] M. Cautun, R. van de Weygaert, B. J. T. Jones, and C. S. Frenk, "Evolution of the cosmic web," *Monthly Notices of the Royal Astronomical Society*, vol. 441, p. 2923–2973, May 2014.

[11] P. B. Alcock, C., "An evolution free test for non-zero cosmological constant," *Nature*, vol. 281, p. 358, Oct. 1979.

[12] P. J. E. Peebles, *Principles of Physical Cosmology*. 1993.

[13] B. Ryden, *Introduction to cosmology*. 2003.

[14] V. Icke, "Voids and filaments," *Monthly Notices of the Royal Astronomical Society*, vol. 206, pp. 1P–3P, 01 1984.

[15] M. C. Cautun and R. van de Weygaert, "The dtfe public software: The delaunay tessellation field estimator code," 2019.

[16] B. S. Ryden and A. L. Melott, "Voids in real space and in redshift space," *The Astrophysical Journal*, vol. 470, p. 160, Oct. 1996.

[17] D. Nelson, A. Pillepich, S. Genel, M. Vogelsberger, V. Springel, P. Torrey, V. Rodriguez-Gomez, D. Sijacki, G. F. Snyder, B. Griffen, F. Marinacci, L. Blecha, L. Sales, D. Xu, and L. Hernquist, "The illustris simulation: Public data release," *Astronomy and Computing*, vol. 13, pp. 12–37, Nov. 2015.

[18] M. Vogelsberger, S. Genel, V. Springel, P. Torrey, D. Sijacki, D. Xu, G. Snyder, S. Bird, D. Nelson, and L. Hernquist, "Properties of galaxies reproduced by a hydrodynamic simulation," , vol. 509, pp. 177–182, May 2014.

[19] R. van de Weygaert and W. Schaap, *Tessellation Reconstruction Techniques*, p. 268–275. Springer-Verlag.

[20] R. van de Weygaert and W. Schaap, *The Cosmic Web: Geometric Analysis*, p. 291–413. Springer Berlin Heidelberg, 2008.

[21] E. Platen, R. Van De Weygaert, and B. J. T. Jones, "A cosmic watershed: the wvf void detection technique," *Monthly Notices of the Royal Astronomical Society*, vol. 380, p. 551–570, Sept. 2007.

[22] M. C. Neyrinck, "zobov: a parameter-free void-finding algorithm," *Monthly Notices of the Royal Astronomical Society*, vol. 386, p. 2101–2109, June 2008.

[23] J. M. Colberg, F. Pearce, C. Foster, E. Platen, R. Brunino, M. Neyrinck, S. Basilakos, A. Fairall, H. Feldman, S. Gottlöber, O. Hahn, F. Hoyle, V. Müller, L. Nelson, M. Plionis, C. Porciani, S. Shandarin, M. S. Vogeley, and R. van de Weygaert, "The aspen–amsterdam void finder comparison project," *Monthly Notices of the Royal Astronomical Society*, vol. 387, p. 933–944, June 2008.

[24] E. G. P. Bos, R. van de Weygaert, K. Dolag, and V. Pettorino, "The darkness that shaped the void: dark energy and cosmic voids: The darkness that shaped the void," *Monthly Notices of the Royal Astronomical Society*, vol. 426, p. 440–461, Sept. 2012.

[25] J. Lee and D. Park, "Constraining the dark energy equation of state with cosmic voids," *The Astrophysical Journal*, vol. 696, p. L10–L12, Apr. 2009.

Appendices

A: Kolmogorov–Smirnov test

We compute the Kolmogorov–Smirnov test for given distributions of ellipticity, prolateness and volumes across different redshifts and centerings. While the results for ellipticity and prolateness fall within reasonable lines, the volume results are incredibly unlikely, suggesting a systematic error in volume computation, or the computation of the Kolmogorov–Smirnov test itself.

D_ε; p_ε	D_1	D_2	D_3	p_1	p_2	p_3
$z = 0$	0.0282	0.0246	0.0235	0.5205	0.6946	0.7485
$z = 0.06$	0.0273	0.0216	0.0382	0.5559	0.8327	0.1733
$z = 0.13$	0.0291	0.0341	0.0452	0.4729	0.2864	0.0646
$z = 0.2$	0.0294	0.0303	0.0323	0.4537	0.4094	0.3373
$z = 0.27$	0.0315	0.0227	0.0387	0.3621	0.7674	0.1499
$z = 0.36$	0.0406	0.0386	0.0365	0.1116	0.1504	0.1934
$z = 0.46$	0.0338	0.036	0.032	0.2629	0.1999	0.3321
$z = 0.58$	0.0284	0.0323	0.0404	0.464	0.3053	0.1049
$z = 0.7$	0.0403	0.045	0.0515	0.1058	0.05	0.0159
$z = 0.85$	0.0308	0.044	0.0495	0.3443	0.054	0.0221

Table 7: Kolmogorov–Smirnov test results for ellipticity (ε) CDFs. D_i denotes the Kolmogorov–Smirnov statistic, which measures the maximum difference between the physical and redshift space distributions. The p_i variable denotes the p-value of the test. Which choose a p value threshold at 0.05, where any p-value above it suggests that the two compared distributions are distinct. We note that while the p-value for almost all the CDFs is high, the actual statistic remains fairly low at the 10^{-2} order of magnitude.

D_α; p_α	D_1	D_2	D_3	p_1	p_2	p_3
$z = 0$	0.0264	0.0234	0.0253	0.606	0.7518	0.6618
$z = 0.06$	0.0315	0.018	0.0257	0.3744	0.9505	0.6392
$z = 0.13$	0.0208	0.0257	0.0178	0.8596	0.6389	0.952
$z = 0.2$	0.0253	0.0338	0.0288	0.6481	0.2802	0.4817
$z = 0.27$	0.014	0.0186	0.0173	0.996	0.9267	0.9576
$z = 0.36$	0.0269	0.0432	0.0188	0.5522	0.0782	0.9156
$z = 0.46$	0.027	0.0236	0.0188	0.5355	0.7045	0.9151
$z = 0.58$	0.0173	0.0262	0.0205	0.9519	0.5691	0.8435
$z = 0.7$	0.0298	0.0313	0.0203	0.3973	0.335	0.848
$z = 0.85$	0.0248	0.0333	0.0316	0.6175	0.2533	0.3195

Table 8: Kolmogorov–Smirnov test results for prolateness (α) CDFs. D_i denotes the Kolmogorov–Smirnov statistic, which measures the maximum difference between the physical and redshift space distributions. The p_i variable denotes the p-value of the test. Which choose a p value threshold at 0.05, where any p-value above it suggests that the two compared distributions are distinct. Similarly to the previous table, the p-values indicate the physical and redshift distributions are distinct, but do not differ by much.

D_V; p_V	D_1	D_2	D_3	p_1	p_2	p_3
$z = 0$	1.20E-01	8.79E-11	1.31E-01	7.73E-13	1.53E-01	2.14E-17
$z = 0.06$	1.25E-01	7.85E-12	1.37E-01	5.55E-14	1.45E-01	8.73E-16
$z = 0.13$	1.24E-01	1.25E-11	1.37E-01	4.54E-14	1.52E-01	2.90E-17
$z = 0.2$	1.37E-01	3.19E-14	1.48E-01	1.07E-16	1.53E-01	1.02E-17
$z = 0.27$	1.29E-01	9.83E-13	1.47E-01	1.50E-16	1.63E-01	1.95E-20
$z = 0.36$	1.40E-01	2.86E-15	1.46E-01	1.68E-16	1.61E-01	2.45E-20
$z = 0.46$	1.27E-01	6.04E-13	1.41E-01	9.93E-16	1.63E-01	8.47E-21
$z = 0.58$	1.29E-01	2.32E-13	1.38E-01	2.29E-15	1.55E-01	2.50E-19
$z = 0.7$	1.27E-01	3.97E-13	1.35E-01	6.99E-15	1.55E-01	1.14E-19
$z = 0.85$	1.29E-01	9.66E-14	1.34E-01	4.82E-15	1.44E-01	4.51E-17

Table 9: Kolmogorov–Smirnov test results for volume (V) CDFs. D_i denotes the Kolmogorov–Smirnov statistic, which measures the maximum difference between the physical and redshift space distributions. The p_i variable denotes the p-value of the test. Which choose a p value threshold at 0.05, where any p-value above it suggests that the two compared distributions are distinct. The presented values are exceptionally, and unrealistically low, suggesting a systematic error in volume analysis, rather than no difference between physical and redshift space distribtuions.

B: Illustris unit conversion

As the Illustris units presented on the main website are somewhat confusingly framed, we make sure to include the unit conversion used to produce our results. First, we ignore the h^{-1} factor present in the coordinate data, as it is only there to provide information about the simulation Hubble parameter.

We convert the [ckpc] units to [cMpc] by introducing a factor of 10^{-3}; we do not change the units to proper distance, as using comoving distances will prove useful in later calculations. As for the velocities, we convert them to peculiar velocities by multiplying the values by $\sqrt{a}$ as instructed. However, to match the comoving units in the coordinate data, we also divide by a, hence the operation is equivalent to dividing by $\sqrt{a}$. We can check whether these units match by considering equation (20).